DETECTING THE EFFECTS OF SOIL MOISTURE AND HOT SPOT SIZE ON GEOTHERMAL ANOMALIES VIA REMOTE SENSING TECHNIQUES

JAMES VARGHESE
February, 2016

SUPERVISORS:
Dr. Christoph Hecker
Dr. Janneke Ettema
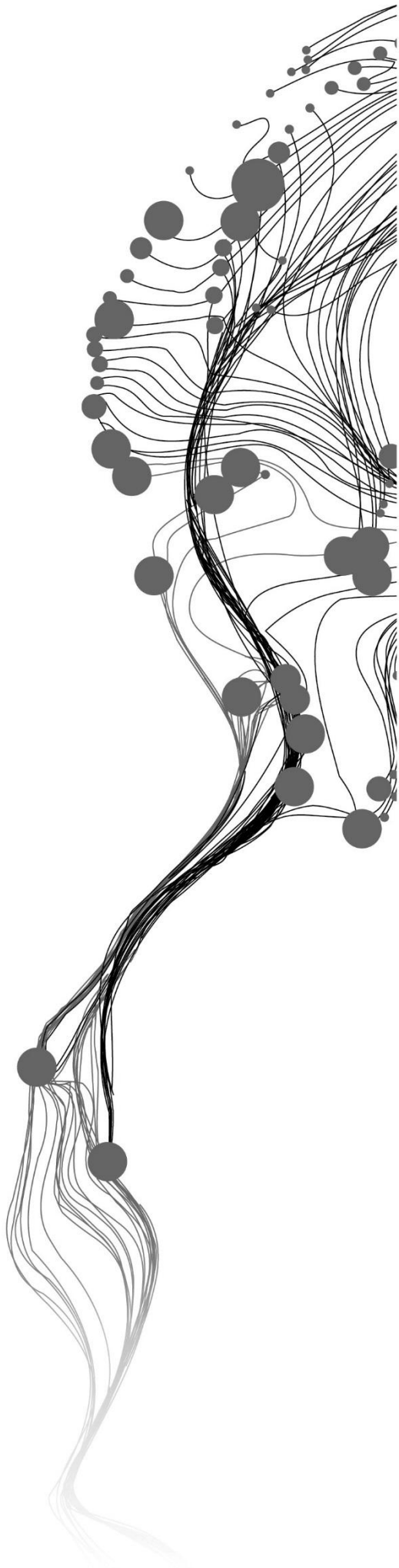
DETECTING THE EFFECTS OF SOIL MOISTURE AND HOT SPOT SIZE ON GEOTHERMAL ANOMALIES VIA REMOTE SENSING TECHNIQUES

JAMES VARGHESE
Enschede, The Netherlands, February, 2016

ABSTRACT

Estimating the influence of soil moisture on geothermal anomalies in remotely sensed thermal infrared data can be a worthwhile pursuit in reconnaissance stage of geothermal energy exploration. Such an activity can assist in making informed decisions while selecting suitable sites for preliminary survey.

Previous studies have examined the effects of topographic slope, albedo, thermal inertia, altitude, sun's heating effects on geothermal anomaly detection. Ways have been found to minimize the number of false anomalies in order to highlight the radiation emitted from geothermal surfaces. However, the effects of soil moisture, especially the changes in emissivity due to variation in soil moisture in sub pixel geothermal anomalies have been poorly understood so far.

This study focused on creating a synthetic model for sub-pixel and soil moisture related thermal anomaly detection using measured and remotely sensed soil information as input. Two types of soils were measured spectrally in dry and wet conditions in the laboratory using an FTIR to extract their emissivity values and later resampled to the ASTER TIR wavelength of 8 to 12μm range. The extreme cases of dry and wet soil emissivity values were used together with Planck's function in the Synthetic Model with a number of remote sensing techniques to generate surface temperature anomaly detection plots. In the model 16 combinations of dry and wet soils were tested associated with temperatures of anomalous and background areas. Additionally, remote sensing datasets of ASTER were correlated with soil moisture data from ASCAT Metop satellite to see whether there was relation between modelled and real-time soil moisture while detecting thermal anomalies.

The lab measurements showed that in general emissivity of soils (sandy loam and loam) increases with moisture content. The variation is higher in the reststrahlen bands as compared to the 11-12μm. Moreover, loam soil showed slight increase in emissivity after further drying out, possibly due to formation of cracks on the surface of the soil.

From the synthetic model investigations of the soil moisture related thermal anomalies, it was deduced that the best detection rates are achieved when the anomalous pixel (high temperature) is covered by saturated soils (high emissivity) and the background (low temperature) with dry soils (low emissivity). This is because surface emitted radiance contrast between the anomalous pixel and the background pixels are developed clearly in order to be detectable. The lowest thermal anomaly detection rates are expected with the reversal of scenario when the anomalous pixel is covered with dry state of soil and the background with wet soil. It was also found from the modelling results that night time conditions are clearly suitable for thermal anomaly detection compared to day time. The ASTER sensor noise had little effect on anomaly detection.

By comparing remotely sensed soil states between known geothermal (anomalous) and non-geothermal (background) regions in Yellowstone Park (USA), helped in understanding modelled detection levels. Time series analysis of 7 cloud free day and night ASTER scenes and ASCAT Metop soil moisture remote sensing data showed that the highest surface temperature anomalies are observed during the lowest relative soil moisture states in night time images. Relatively dry conditions over both geothermal and background area elevates the thermally emissive areas' emitted radiance with respect to not so emissive background area. However, when the background and anomalous pixels are equally wet, there is less emitted radiance contrast between the background and anomalous pixels compared to when the conditions are dry. The spectrally emitted surface radiance differences between anomalous and background area were found to be higher in night time than in day time, supporting the modelled result that night time images are better suited for detecting geothermal anomalies. The synthetic model results can be extrapolated to remote sensing results because the input parameters for the synthetic model are based on realistic temperatures and emissivities. The uncertainties are quite large with remote sensing data analysis as the time of acquisition of Soil Moisture and TIR data by ASCAT and ASTER have differences of more than 5 hours in addition to disparity in spatial resolutions of 25 km and 90 m respectively. Moreover, uncertainties are compounded due to the fact that soil moisture states are quite dynamic processes affected by subtle fluctuations in meteorological, hydrological as well as land processes such as geothermal activities, amongst others.

This study showed that the best time to look for geothermal anomalies in remotely sensed ASTER TIR data is during clear cloud free night time skies with low soil moisture states. However, if there is possibility to identify separately the soil moisture conditions of anomalous and background area, then the best thermal anomaly detection rates are expected when the anomalous pixels are saturated with soil moisture with high temperature and the background pixels completely dry with low temperature.

Key words*: Geothermal Anomalies, Sub-pixel, Soil Moisture, Emissivity, Land Surface Temperature, Emitted Radiance, Thermal Infrared, Remote Sensing, Thermal Anomalies, FTIR, ASTER, ASCAT Metop, Synthetic data model*

ACKNOWLEDGEMENTS

TABLE OF CONTENTS

LIST OF FIGURES

LIST OF TABLES

1. INTRODUCTION

1.1. The Greater Context

Geothermal energy stored within the earth can be considered a boon as well as a bane. A boon because the abundant geothermal heat energy can be used together with other renewable sources such as hydropower, solar, wind, biomass, tidal energy to meet the energy demands in various parts of the world. Additionally, many non-renewable energy resources are progressing towards exhaustion and due to that there is a compelling need to shift the focus on renewable sources of energy. More importantly, the need for renewables is pressing because polluting sources such as fossil fuels are one of the main factors for the alarming rise in green house gas emissions which in turn aggravates climate change. The Dec. 2015 historic agreement among nations of the world in Paris Climate Conference – COP 21 (UNEP, 2015) is an example of how committed the world is in mitigating climate change. A bane because the same source of sub surface heat energy can sometimes cause disastrous consequences in the form of volcanic hazards (Abrams et al., 2015). Since most of the geothermal sources around the world are in some way associated with volcanic hot spots, therefore geothermal sources can also indirectly hint towards volcanic hazards.

Geothermal energy exploration begins with pinpointing locations of geothermal anomalies. Identifying geothermal surface anomalies in remote sensing datasets could be a logical step towards geothermal resource exploration. Remote sensing provides a better overview for early stage of prospecting compared to a person on the ground with limited field of view. Particularly with remote sensing, temperature anomalies associated with geothermal features are the prime target for an energy explorer, in addition to classifying mineralogical anomalies. Based on thermal anomaly maps together with ancillary information, field teams can equip themselves to concentrate on a narrow zone of survey for further ground based exploration.

Geothermal anomalies in remote sensing datasets can be influenced by external factors such as sun's heating effects, atmospheric conditions and land surface states. Some external components such as sun's heating effects have been studied in the past and ways have been found to minimize their undesirable effects. However, the effects of land surface states, particularly the effects of soil moisture on geothermal anomalies have not been clearly studied yet. Therefore this study scrutinizes the effects of soil moisture and its implication on geothermal surface anomalies with the aid of remote sensing techniques. This study also includes spectral measurements of dry and wet soils in the lab. The lab results are then integrated into a synthetic data model for analyzing the influence of soil moisture in anomaly detection. Remote sensing satellite datasets are also examined for possible clues to soil moisture affected geothermal anomalies.

1.2. Geothermal Anomalies

Definition of geothermal anomalies

Geothermal surface anomalies have been described by various studies in different ways. In this study geothermal surface anomalies are described as temperature related anomalies which are associated with geothermal features such as hot springs, geysers, hot grounds and fumaroles on the surface of the earth following the description by Haselwimmer & Prakash (2013). Generally, the locations of these geothermal anomalies are characterized by higher temperature or heat emissions with respect to its surrounding.

Genesis of geothermal anomalies

Geothermal surface anomalies are surface expressions of sub-surface heat energy of the earth. This heat energy finds its way through gaps in between plate boundaries; particularly near intra-plate hotspots, convergent, divergent (Heasler et al., 2009) and transform plate margins. Normally, geothermal temperature gradient is around 25-30°C/km on the Earth's crust but in places near the plate margins they can be as high as 150°C/km (van der Meer et al., 2014). Heat energy from inside reaches the surface by a series of convection and conduction mechanisms. Moreover, there is a sub-surface interaction of heat, fluids and rock which ultimately manifests itself on the surface in the form of geothermal surface manifestations such as hot springs, geysers, steam vents, hot grounds and mud pots. These geothermal features exhibit gases as well as fluids in combination with heat (Haselwimmer & Prakash, 2013) on the surface which is recognized as characteristic features of geothermal systems. Some of the examples of geothermal locations around the world are Yellowstone National Park (YNP) in the United States, parts of Indonesia and East African rift.

Applications of geothermal anomalies

Apart from aesthetic reasons, there are two other rationales for studying these intriguing natural phenomena. Firstly, in geothermal prospecting, identifying geothermal surface anomalies with remote sensing techniques is a pragmatic step towards geothermal resource identification (Haselwimmer & Prakash, 2013; Reath & Ramsey, 2013). During preliminary phase of geothermal energy exploration, locating potential sites for further ground based surveys and exploration can save cost (Haselwimmer & Prakash, 2013), effort and time.

The second reason for locating geothermal surface anomalies via space based remote sensing is for hazard monitoring. Monitoring geothermal surface anomalies can potentially hint towards abnormal sub-surface magmatic activities or impending hazards associated with volcanic-geothermal systems. In effect, geothermal anomalies have the potential of raising an early warning signal (Dehn et al., 2002; Pergola et al., 2009; Pieri & Abrams, 2005; Vaughan & Hook, 2006; Wessels et al., 2013).

Remote sensing of geothermal anomalies

In order to map geothermal surface anomalies, remote sensing has been used widely for a number of decades. The primary advantage of using remote sensing techniques has been to lessen the cost and effort for ground based surveys in large and inaccessible locations for geothermal prospecting(Calvin et al., 2005). Especially thermal infrared (TIR) remote sensing has been used for mapping geothermal surface temperature, heat flux and mineral anomalies (Coolbaugh et al., 2007; Haselwimmer & Prakash, 2013). The TIR range between 8-14 μm is particularly useful because of the following three reasons. 1) there is a good atmospheric window in this range for remote sensing of terrestrial features, 2) the peak radiation of terrestrial objects with temperatures between -66 °C to less than 100 °C occurs in this 8-14μm wavelength range, 3) many minerals such as quartz and feldspars with exception of clay minerals have diagnostic features in the 8-14μm wavelength region which helps to identify the kind of material a surface is made of (Gupta, 2003). A particularly well suited application of remote sensing has been to map surface thermal anomalies associated with finding geothermal resources for energy development. A lot of work has been done in the US using aerial photographs and satellite imagery for geologic and thermal anomaly mapping respectively for geothermal energy exploration (Moore et al., 2006).

Applications of airborne remote sensing

Pioneering studies were done in the 70's with airborne remote sensing, notably thermal infrared (TIR) remote sensing. TIR remote sensing is uniquely applicable for geothermal surface anomaly mapping because it can help to detect surface temperature anomalies, heat flux anomalies and for mineral indicators

associated with geothermal systems (Haselwimmer & Prakash, 2013). Thermal anomaly mapping was used in selecting sites for further geothermal prospecting and exploration. The results of TIR remote sensing were coupled with conventional ground based methods such as magnetic, gravity and ground temperature measurements to validate the feasibility of airborne remote sensing. Costs for exploring potential geothermal resources were cut down as the number of possible sites for drilling was reduced after applying air borne TIR remote sensing (Hochstein & Dickinson, 1970; Hodder, 1970). Decades later after much advancements in sensor technologies, high resolution (3m) TIR remote sensing was used to map geothermal surface temperature anomalies within the wavelength range of $8.4 - 11.6\ \mu m$ (Mongillo, 1994) This wavelength range is interesting because it used in sensing the surface emitted energy (Kuenzer & Dech, 2013). TIR remote sensing technique also successfully identified and mapped previously unknown geothermal hot spots. Results showed close match with ground measurements (Mongillo, 1994).

Applications of satellite remote sensing

High resolution (<5m) TIR airborne sensors are ideal for mapping and monitoring geothermal surface anomalies as the sizes of geothermal features are relatively small compared to the background. Moreover, the temperature differences may not be very high either (Haselwimmer & Prakash, 2013). However, due to constraints in cost, spatial extent and temporal coverage freely available satellite sensors with TIR capabilities are preferred.

Satellite remote sensing has been used extensively in numerous studies for mapping geothermal resources and also for monitoring activities. Land Surface Temperature (LST) is a common indicator for many geothermal-volcanic studies (Li et al., 2013; Tianyu et al., 2012). In China a research was carried out using Landsat ETM+ TIR data to calculate the LST of a geothermal area using the single channel algorithm. The temperature of the background region was deducted from the temperature of the geothermal feature to analyze the temperature anomaly (Qin et al., 2011).

Issues of false positives

In spite of many studies with TIR remote sensing the identification of geothermal surface anomalies are not so straightforward. The main reason is the contamination of geothermal heat with other sources of heat energy, especially sun's heating effects. In order to isolate the effects of sub-surface geothermal heat in remotely sensed satellite images external effects of non-geothermal sources otherwise called false positives have to be discarded (Coolbaugh et al., 2007). To quantitatively characterize geothermal surface anomalies, two indicators are generally used namely, geothermal heat flux (GHF) (Vaughan et al., 2012) and surface (skin) temperature (Coolbaugh et al., 2007). In using either of the indicators the intention is to eliminate the predominant effects of other sources of heat and focus on geothermal related anomalies. Although there have been a number of studies related to false positive elimination in the context of remote sensing of geothermal exploration and volcano-geothermal monitoring, only some of them are listed here for the sake of focusing on the most relevant false positives pertinent to this research.

i) Topographic effects (Gutiérrez et al., 2012; Coolbaugh et al., 2007)
ii) albedo effects (Coolbaugh et al., 2007),
iii) thermal inertia effects (Coolbaugh et al., 2007),
iv) soil moisture and vegetation effects (Coolbaugh et al., 2007).

The following sections outline specific studies which tackled some of the false positives and the limitations of their study.

Studies related to surface temperature anomalies and their strengths

In a study carried out in Nevada, US, Coolbaugh et al. (2007) used ASTER TIR (90m) satellite data to determine the surface temperature anomalies associated with geothermal features by minimizing a number of false positives. Specifically, the false temperature anomalies associated with day and night heating of the sun such as effects of albedo, thermal inertia, topographic slope, and emissivity were dealt with. A DEM was used to rectify the temperature effects caused due to topographic slope. For correcting the temperature effects produced due to albedo, they utilized the visible and near infrared bands of ASTER. Thermal Inertia is dependent on three factors, thermal conductivity, density and heat capacity of an object (Elachi & Zyl, 1987). Coolbaugh et al. (2007) minimized the effects of thermal inertia by taking the average temperature of day and night derived from the surface kinetic temperature product of ASTER and by calibrating it with the in situ temperature measurements taken on the ground. Emissivity does not depend on temperature but its value is affected by the properties of the material such as variations in soil moisture, changes in land cover. It is also dependent on wavelength (Kuenzer & Dech, 2013). In the study by Coolbaugh et al.(2007) temperature corrections were taken care by ordering the AST_08 surface kinetic temperature product and by comparing it with ground measurements of temperature to see whether the deviations were within the acceptable limits (Coolbaugh et al., 2007). AST_08 applies the Temperature Emissivity Separation (TES) algorithm which is based on 5 TIR bands of ASTER.

A similar study (Gutiérrez et al., 2012) was carried out in Chile, South America in a geothermal area in the Andes mountain range which built on the methodology of Coolbaugh et al., (2007). In addition, they looked at the factor of temperature variations due to elevation as a false positive. Gutiérrez et al., (2012) came up with a modelling technique to account for the temperature changes by corrections involving ground measurements.

Limitations of the study

Although, the methodology followed by Coolbaugh et al. (2007) minimized the false positives and was able to highlight the contributions of geothermal surface anomalies, still the effects of soil moisture was ignored as it was a relatively dry area. This effect cannot be neglected in areas where the effects of soil moisture and vegetation are substantial (Haselwimmer & Prakash, 2013). As a consequence, important components from the energy balance equation such as sensible heat and latent heat were ignored and the equation was simplified in this study (Coolbaugh et al., 2007). In addition the soil moisture content was described as causing cooler temperature effects relatively without quantification.

Study related to geothermal heat flux mapping and their strengths

Researchers from USGS and Yellowstone National Park (Vaughan et al., 2012) worked with a combination of higher spatial resolution TIR satellite imagery of Advanced Spaceborne Thermal Emission and Reflection Radiometer (ASTER (90m)) and lower spatial but high temporal resolution of Moderate Resolution Imaging Spectroradiometer (MODIS (1km)) sensors. The specific purpose of using these sensors in Yellowstone was to monitor different kinds of geothermal areas by quantifying their geothermal heat flux and to determine any subtle thermal changes in their activity. MODIS time series data was used to visualize the seasonal thermal variations of background areas surrounding the geothermal features and ASTER data was used to estimate the geothermal heat flux of individual geothermal features and also of the whole area (Vaughan et al., 2012). This research made it possible to identify when a thermal anomaly is related to normal seasonal changes and when it can be related to geothermal activity, which is crucial information for long term geothermal and volcano monitoring studies.

Limitations of the study

Even though ASTER and MODIS were useful for this study the question of how long they would be operational is an urgent one; therefore new and alternative tools and sensors have to be utilized. Secondly, the decision of subjectively defining the background region with respect to the thermal region (Vaughan et

al., 2012) may have imported some biases while identifying geothermal anomalies. In this study visual comparison was the basis for defining the background region and was not based on any automated way.

1.3.   Research Problem

This research focuses to understand the effects of soil moisture while detecting geothermal surface temperature anomalies with remote sensing techniques. It is not understood how soil moisture influences the emitted radiance in the 8 to 12 μm TIR range. Particularly, the effects of changes in emissivity caused due to variation in soil moisture have not been explored by previous studies in the context of geothermal surface anomaly detection. In the research mentioned earlier, the study areas were mostly situated in semi-arid regions or the study was conducted in dry areas (Coolbaugh et al., 2007) where there was least effect of moisture. In a contrary situation when soil moisture has significant contribution, the essential sources of heat in the surface energy balance equation such as latent heat and sensible heat fluxes are active. Additionally, geothermal anomalies can usually be sub-pixel (Haselwimmer & Prakash, 2013) in size when compared to a 90m ASTER TIR pixel. To deal with the issue of soil moisture impact, sub-pixel mixing and subjective background selection while detecting thermal anomalies associated with geothermal features, a synthetic data analysis is conducted with the support of remote sensing and modelling techniques. Additionally, this study also experimented with a sub-pixel linear spectral mixing analysis technique.

By addressing the research problem, this study tried to find appropriate ways to detect geothermal surface anomalies with remote sensing techniques while taking into account emissivity effects caused due to soil moisture changes. The hypothesis is that soil moisture effects produces cooler anomalies (Coolbaugh et al., 2007). Effects of soil moisture could be fairly large in geothermal areas located in regions with prominent precipitation events. Therefore, one the overarching aims of this study was to examine geothermal anomalies with significant contributions of soil moisture in the top few centimetres of the surface.

1.4.   General Objective:

To examine and quantify the effects of soil moisture in detecting geothermal surface temperature anomalies with remote sensing techniques

1.4.1.   Research Objectives and Research Questions

1. To define a geothermal surface anomaly
    a) What are the typical sizes and temperature differences of geothermal anomalies?

2. To perform synthetic data analysis to simulate the effects of soil moisture in detecting geothermal surface temperature anomalies
    a) Which parameters related to soil moisture can influence the geothermal anomaly detection? (e.g., emissivity, albedo, thermal inertia, latent heat flux etc.)
    b) What is the consequence of satellite sensor noise levels on the detected results using synthetic data analysis?
    c) What are the differences in the day and night conditions?

3. To analyze real remote sensing datasets to examine the effects of soil moisture in detecting geothermal surface temperature anomalies
    a) What are the appropriate data sets and study areas for testing the results achieved from objective 2)?
    b) What are the limitations and uncertainty level to the methods applied in the real data analysis?

1.4.2.   Outline and Structure of next chapters

The structure and outline of chapters and sections are as follows. Chapter 2 begins with the data and study area description. Chapter 3 focuses on methods and results obtained from the thermal infrared measurements of dry and wet soils. Chapter 4 deals with the Synthetic data modelling. It is further broadly divided into two parts. Part A forms the core part of the model and Part B is an extension to the model. Chapter 4 finishes with the results associated with Part A and Part B. Chapter 5 includes methods and results of the time series analysis of remote sensing data to examine the effect of soil moisture in detecting geothermal anomalies. Chapter 6 focuses on discussion. The thesis ends with Chapter 7 and Chapter 8 which are Conclusions of the study and Recommendations for further work respectively.

2. STUDY AREA & DATA DESCRIPTION

The aim of the study area and data description is to collect relevant information for addressing the first research objective of defining a geothermal surface anomaly and this chapter is about the study area and associated data descriptions. It is divided into two sub sections. 2.1 deals with the study area description and 2.2 explains the cataloged data for the study.

2.1. Study Area: Yellowstone & Olkaria

In order to quantify the sizes and temperatures of thermal features and their surroundings two known geothermal locations namely Yellowstone (44°36'N, 110°30'W) in United States and Olkaria (0°46' 6.70"S, 36°21'2.32"E) in Kenya, East Africa were chosen. These two locations were chosen also based on the criteria that they represent two different climatic and geological settings. Yellowstone is part of humid continental climate found within the temperate zone and Olkaria is situated along the equator within the tropics. Yellowstone geothermal areas are the result of Intraplate Volcanism (Bergfeld et al., 2011) while the geothermal areas in Olkaria resulted from the East African Rift (Macgregor, 2015), an example of a continental rift zone. The elevation near Yellowstone lake is 2399 m above sea level. Summer months in Yellowstone begin from June and last until September with the average high air temperature around 19.1°C and the average low around 2.8°C. There are thunderstorms which occur around afternoon time during summer in Yellowstone (NPS, 2016). The average precipitation is 44 mm/day for the summer months (NOAA). The elevation near Lake Naivasha is 1884 m above sea level. The lake is close to Olkaria. Although Kenya falls within the tropical climate zone, the inland regions and higher altitudes make it more temperate type of climate. January to March months are generally hot in Olkaria (Bank, 2016).

To address the research objective of defining a geothermal surface anomaly, Airborne High Resolution Infrared data would have been ideal but due to inaccessibility of such data, information was collected from appropriate literature. Thermal areas present in Yellowstone National Park contain around 10,000 features whose temperatures range from a few tens of degrees Celsius to the boiling point temperatures (~ 94°C because boiling temperatures are lower at higher altitudes of Yellowstone). Their sizes range from some centimetres to 10's of meters (Vaughan et al., 2014). But typically in Yellowstone the thermal areas cluster together and form groups of thermal features. One of the examples is Upper Geyser Basin which is around 2.9 km² formed by many smaller thermal features (Jaworowski et al., 2010). The surface temperature anomaly is the difference in temperature of anomalous thermal features to the background surrounding region associated with geothermal activity. Generally, geothermal areas are characterized by positive thermal anomalies. The temperature of an ASTER TIR pixel in Yellowstone show ranges above 0°C to around 43°C in the ASTER Satellite surface temperature image; one of the hottest thermal areas are found in Sulfur Hills (Vaughan et al., 2014). For areas in and around Olkaria Volcanic Complex in Kenya, the surface temperatures associated with hydrothermal activity was also found to be reaching around the boiling point of 94 °C at that altitude. The sizes of geothermal anomalies here range in km., because these anomalies are found generally along faults or cracks or along volcanic rims which can be up to 10's of km. Information regarding geothermal areas in the south part of the East Africa Rift Valley in Kenya was retrieved from Geothermal activity map of Olkaria and adjacent areas (Clarke et al.,1990).

Yellowstone National Park, US
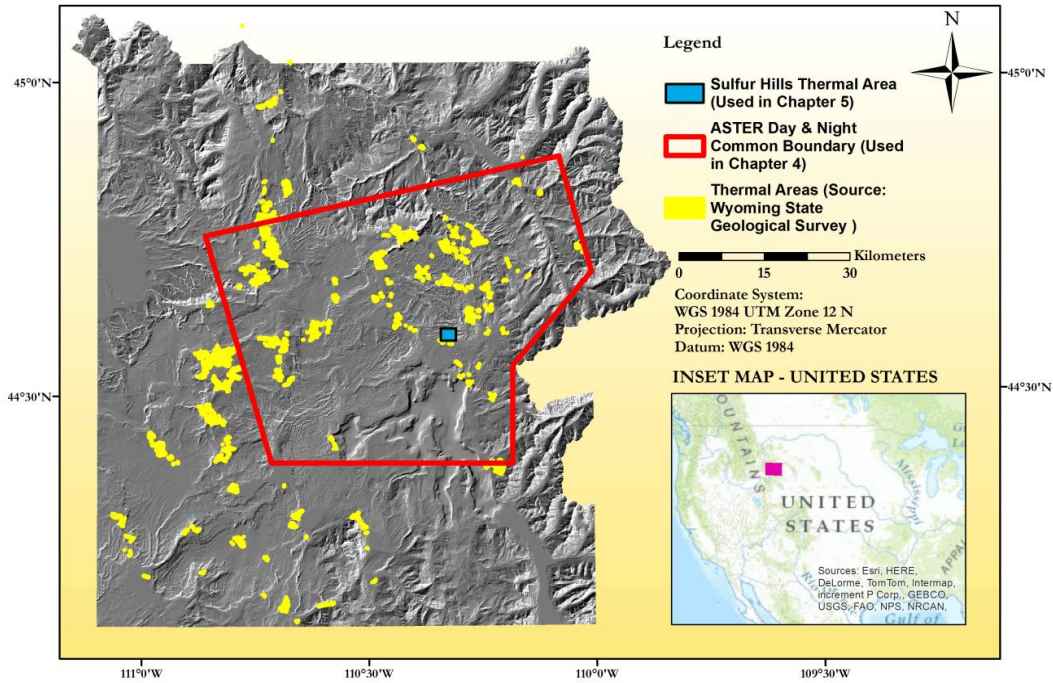
Figure 1 Yellowstone National Park study area map. The map shows thermal areas in yellow colour overlaid on a hill shaded digital terrain model. The day and night common ASTER image boundary shown with a red polygon was used for background area delineation in Chapter4. The thermal area used in Chapter 5 for the times series analysis is demarcated by the blue coloured region with black outline.

Olkaria, Kenya
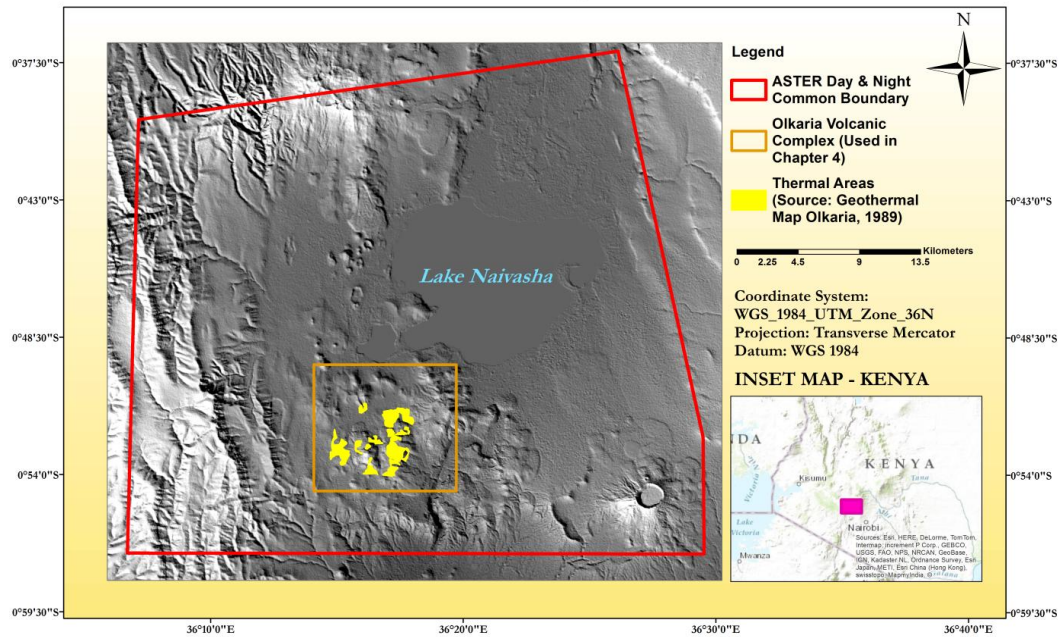
Figure 2 Olkaria Geothermal Region study area map. The map shows Olkaria Volcanic Complex outlined in orange square box overlaid on a hill shaded digital terrain model lying south of lake Naivasha. The thermal areas are marked in yellow colour. The area within the red polygon is the common boundary of day and night ASTER image. Olkaria Volcanic complex was used in Chapter 4 for background area digitization.

Yellowstone study area map in Figure 1 highlights the thermal areas in yellow colour. The source of thermal area is GIS data from Wyoming Sate Geological Survey (Ranz, 2015) website. The red outline in the map shows the overlapping areas of day and night ASTER satellite images. Within this overlapping boundary of ASTER image surface temperatures of thermal areas and their surrounding areas were analysed. Subsequently the background regions were digitized. The rationale for extracting surface temperatures from the surrounding background regions will be explained further in Chapter 4.

For Olkaria, study area map shown in Figure 2, the thermal areas were digitized based on an old Geothermal map of Olkaria, Kenya from 1989 (Ledgard, 1989). This was the only reference map available for locating the thermal areas. However, it can be seen from recent satellite and Google Earth Imagery that most of the areas covered by thermal area on the 1989 map are now mostly occupied by geothermal power plants. Therefore the location of thermal features on the study area map in Figure 2 is uncertain.

2.2.   Data Description

In order to assess the Land Surface Temperatures of the two geothermal areas in remotely sensed data in the thermal infrared wavelength range (8 to 12 μm) ASTER Satellite Images were chosen. ASTER stands out among all freely available space based sensors especially because of its 5 thermal (90m) bands including 4 visible-near infrared (15m) bands and 6 shortwave infrared (30m) bands (Abrams et al., 2015). With 5 thermal bands temperature and emissivity can be estimated using Temperature Emissivity Separation (TES) algorithm which provides information about thermal and compositional properties of an object on the ground (Gillespie et al., 1998). As a consequence, numerous studies were carried out to exploit ASTER's unique capabilities and were successfully applied in geothermal exploration and a number of volcano monitoring studies (Abrams et al., 2015; Calvin et al., 2002; Davies et al., 2008; Eneva et al., 2007; Eneva et al., 2006; Eneva & Coolbaugh, 2009; Murphy et al., 2011; Vaughan et al., 2010; Vaughan et al., 2008).

In this study three products of ASTER namely Surface Kinetic Temperature, Emissivity and Surface Radiance TIR were ordered from LPDAAC in order to quantify the surface temperature, emissivity and emitted radiance of surrounding background region and geothermal region. The In situ geothermal hot spot temperatures were also needed in order to quantify the sizes of geothermal surface temperature anomalies. GIS data of geothermal areas were useful in ascertaining the location of known thermal areas. Precipitation and relative soil moisture data were required to examine the relationship of soil moisture with thermal anomalies. In addition, emissivity measurements of dry and wet soil were also required for synthetic modelling purposes which will be described in detail in the next chapter. Table 1 shows the sources of Day and Night Satellite Land Surface Temperature, Land Surface Emissivity, Surface TIR Radiance, Daily Precipitation and Relative Soil Moisture Data. Table 1 also summarizes the source of information on In situ thermal area temperatures, Soil data and GIS data. For Yellowstone all the data types shown in Table 1 are applicable for the study but for Olkaria only Surface Kinetic Temperature and In situ hot spot temperatures were collected. The surface temperature and in situ hot spot temperatures for Olkaria were only used in Chapter 4 to extract background temperatures and anomaly detection respectively. Yellowstone data was used both in Chapter 4 and Chapter 5 for anomaly detection and time series data analysis respectively.

Table 1 Collected Data Summary associated with Yellowstone and Olkaria. Data Type is the column heading for name of the data, Data Code column stands for specific ASTER On demand product codes, Time Period column shows the time period of the data acquisition, the Location column shows the area of data acquisition, and the Service Provider column indicates the name of the agency which provided the data.

Data Type	Data Code	Time Period	Location	Service Provider
ASTER Surface Kinetic Temperature	AST_08	June 2012 - Sept 2012	Yellowstone, Olkaria	LPDAAC, NASA, USGS
ASTER Emissivity	AST_05	June 2012 - Sept 2012	Yellowstone	LPDAAC, NASA, USGS
ASTER Surface Radiance TIR	AST_09T	June 2012 - Sept 2012	Yellowstone	LPDAAC, NASA, USGS
In situ Hot Spot Temperatures	-	2003-2012, 1989	Yellowstone, Olkaria	Montana State University, Olkaria Geothermal Map
Sandy Loam & Loam Soils	-	2015	Netherlands	ITC, University of Twente
Precipitation	-	Daily Summaries (June to Sept. 2012)	Yellowstone	NOAA
Relative Soil Moisture - ASCAT Metop	-	Almost Daily (June to Sept. 2012) with time gaps	Yellowstone	TU Wien (Austria)
GIS Data of thermal areas	-	-	Yellowstone	Wyoming State Geological Survey

3. THERMAL INFRARED MEASUREMENTS OF DRY AND WET SOIL

The main aim of the thermal infrared measurements of dry and wet soil in the laboratory was to assess the impact of soil moisture on TIR. By subsequently using extreme cases of dry and wet soil emissivity in the synthetic data modelling analysis the experiment answers the research objective of soil moisture influenced anomalies. This section describes the methods and results of the emissivity measurements which were carried out in the Geoscience Laboratory using Fourier Transform Infrared Spectrometer (FTIR) for two types of soil. The application of the emissivity in the synthetic data model is further described in Chapter 4.

3.1. Methods

The aim with the thermal infrared measurements of dry and wet soil is to extract emissivity values in the thermal infrared wavelength (8 to 12μm). Knowing the emissivity is crucial for correctly estimating the emitted radiance and for determining surface temperature from radiance data. Moreover, in case of geothermal anomalies, relative difference between the background and anomalous surface emissivity can provide useful clues on the type and condition of the surface material. Two soils were used for this study, namely Sandy Loam and Loam Soils. Table 2 provides the textural summaries of soil types used for the emissivity measurements. Sandy Loam is an example of a quartz dominated soil and loam is an example of a soil which has more clayey minerals. A pure clay sample was not available, therefore loam soil was chosen instead.

Table 2 Soil textural information summary.This table shows the summary of the textures of two types of soil, Sandy Loam and Loam with their corresponding textures with Clay(%), Silt (%), Sand (%). Additionally the location of the soils are also included.

Soil Type	Clay (%)	Silt (%)	Sand (%)	Location
Sandy Loam	14.39	11.05	74.56	Deventer, NL
Loam	16.75	44.16	39.09	Limburg, NL

An experimental setup was created in the laboratory using an FTIR (Fourier Transform Infrared Spectrometer) (Hecker et al., 2011). The soils were fully saturated with distilled water. Two Petri dishes were then filled and packed with saturated sandy loam and loam soils to the brim by smearing them with a spatula. This was done to make sure that the saturated soils were equally and homogeneously spread without leaving any empty pores. Beginning with the saturated soils filled to the top of the Petri dishes spectral measurements from 1.4 μm to 16 μm range were taken for both soil types. After each measurement the soils were weighed and dried in a thermostatic oven at 105 °C for 40 minutes each, then left to cool to room temperatures and re-measured in the FTIR. The duration of each day's measurements was approximately from 08:30 until 17:30 hrs. To prevent loss of moisture the Petri dishes containing soil samples were wrapped in a thin plastic foil until the measurements were taken the subsequent day and weighed before and after the measurements. It took three days to reach the dry state of each soil type

beginning from fully saturated states. At the end of the procedure, the soil moisture content was gravimetrically calculated for each of the spectral measurements that were taken.

3.2.   Results

The results section shows the table of the measured soil moisture content of sandy loam and loam soils. In addition the emissivity plots of sandy loam and loam soil are presented with their description.

3.2.1.   Soil Moisture Content Tabular Results

The results of the soil moisture content measurements for sandy loam and loam soils are calculated after every measurement and were recorded in Table 3. The table shows gravimetric soil moisture content (SMC) measurement information from fully saturated states to dry state for both sandy loam and loam soil during the course of the experiment. SMC % column stands for the ratio of weight of water content by the weight of dry soil in %. The resulting emissivity graphs and descriptions are presented in Figure 3 for Sandy Loam and Figure 4 for Loam.

Table 3 Dry and wet Soil Moisture Content (SMC). Summary table of Sandy Loam and Loam Soil. Time column represents time in minutes of drying the soils in the oven. Soil type column stands for the type of soil being measured.

Sr. No.	Drying Time(min)	Soil Type	Petri dish Wt. [g]	Petri dish & Wet Soil Wt. [g]	Petri dish & Dry Soil Wt. [g]	Moisture Wt. [g]	Dry Soil Wt. [g]	SMC [%]
1	Saturated	Sandy Loam	22.06	77.61	62.07	15.54	40.01	38.84
2	40	Sandy Loam	22.06	70.15	62.07	8.08	40.01	20.19
3	80	Sandy Loam	22.06	62.15	62.07	0.08	40.01	0.20
4	120	Sandy Loam	22.06	62.12	62.07	0.05	40.01	0.12
5	160	Sandy Loam	22.06	62.10	62.07	0.03	40.01	0.07
6	200	Sandy Loam	22.06	62.08	62.07	0.01	40.01	0.02
7	240	Sandy Loam	22.06	62.07	62.07	0	40.01	0.00
1	Saturated	Loam	22.2	76.21	61.91	14.3	39.71	36.01
2	40	Loam	22.2	68.17	61.91	6.26	39.71	15.76
3	80	Loam	22.2	63.67	61.91	1.76	39.71	4.43
4	120	Loam	22.2	62.04	61.91	0.13	39.71	0.33
5	160	Loam	22.2	61.94	61.91	0.03	39.71	0.08
6	200	Loam	22.2	61.95	61.91	0.04	39.71	0.10
7	240	Loam	22.2	61.91	61.91	0	39.71	0.00

3.2.2.   Emissivity of Dry & Wet Soils

Figure 3 and Figure 4 depict the emissivity plots corresponding to Soil Moisture Content (SMC) measurements of two different types of soil documented in Table 3. The grey shaded background regions in the plots indicate the positions of 5 ASTER (TIR) Bands (Band 10 to 14). The thick dark blue line in

each plot corresponds to the fully saturated state of soils and the thick red line corresponds to the completely dry state of soils. All other coloured lines show the intermediate soil moisture states of soil. The plots also include the emissivity spectra of distilled water taken from online JHU – JPL ASTER Spectral Library for reference shown with a dashed blue line. Both (Figure 3 and Figure 4) the plots show the changes in emissivity for a soil type.

Sandy Loam

The thick red line in Sandy Loam emissivity plots in Figure 3 shows the state of soil when it is dry. The dominant quartz reststrahlen feature can be clearly identified around 8 and 9 μm range covered by Band 10 to 12 in ASTER TIR. 9.27 μm feature of K feldspar has overshadowed quartz a little bit. The lowest emissivity values in Sandy Loam are found in ASTER TIR Band 10 and Band 12 at 0.88 and the highest values are found in Band 13 and Band 14 at 0.96.

The dark blue line in Figure 3 represents the saturated sandy loam soil condition. The quartz reststrahlen feature is lost and can only be faintly identified. The dominance of moisture in the soil obscures the absorption features of mineral spectra when dry. The wet sandy loam soil has an emissivity of 0.99 in Band 14 of ASTER TIR and the lowest emissivity value of 0.95 in Band 10.

The emissivity plot at 20% SMC shows an intermediate step between the fully saturated and fully dry states of soil. The highest variations are observed in Band 10 and Band 12.
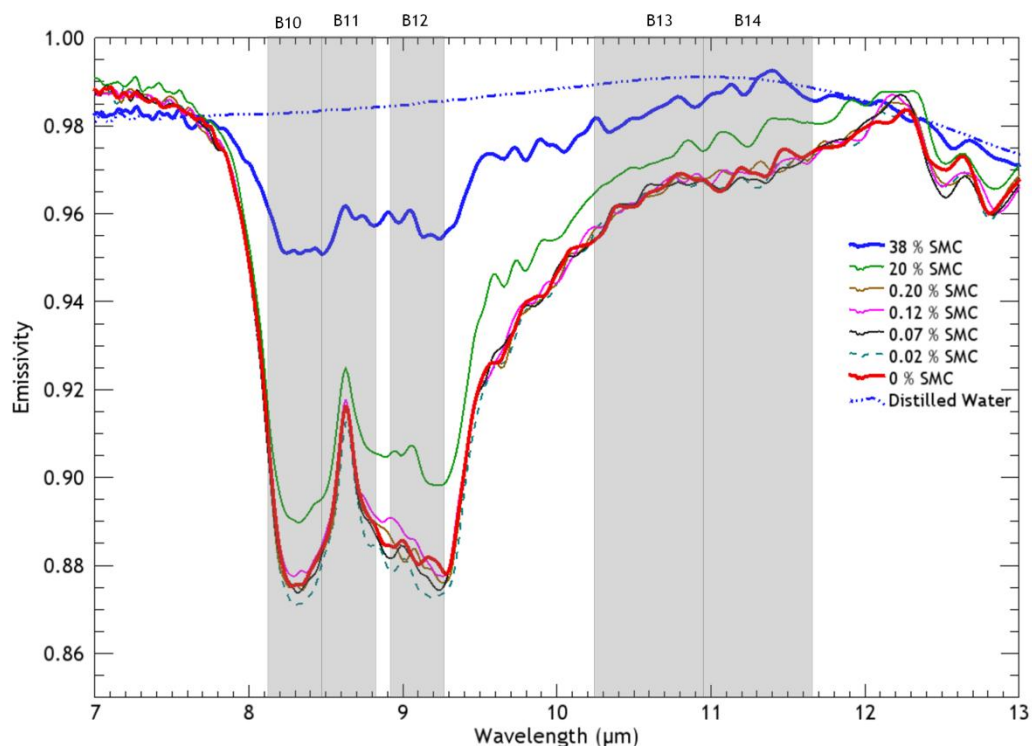
Figure 3 Sandy Loam Soil Emissivity Measurements with changing SMC corresponding to Table 3. The horizontal axis is the wavelength in micrometers (μm) from 7 to 13 μm. The vertical axis is the emissivity with the maximum value of 1. The grey shaded regions are the position of the 5 ASTER TIR bands.

Loam Soil

The thick red line in the Loam emissivity plots in Figure 4 shows the state of soil when it is dry. It is evident that the driest sample does not contain the lowest emissivity in this case. For the dry state at 0% SMC, the highest emissivity of 0.96 is found in Band 14 and the lowest emissivity value of 0.93 is found in

Band 10 in ASTER TIR. The spectral shape of the dry spectrum shows a combination of quartz features (lobe at 8.2 and peak at 8.62) as well as a mixture of clay mineral (probably montmorillonite) and muscovite. At fully saturated state (36% SMC dark blue line) Loam soil showed less variation in emissivity (0.97-0.98) in ASTER TIR. The intermediate plots show that the lowest emissivity values of 0.91 are observed with SMC at 4.43% (green line) in the 8-9μm range of Band 10
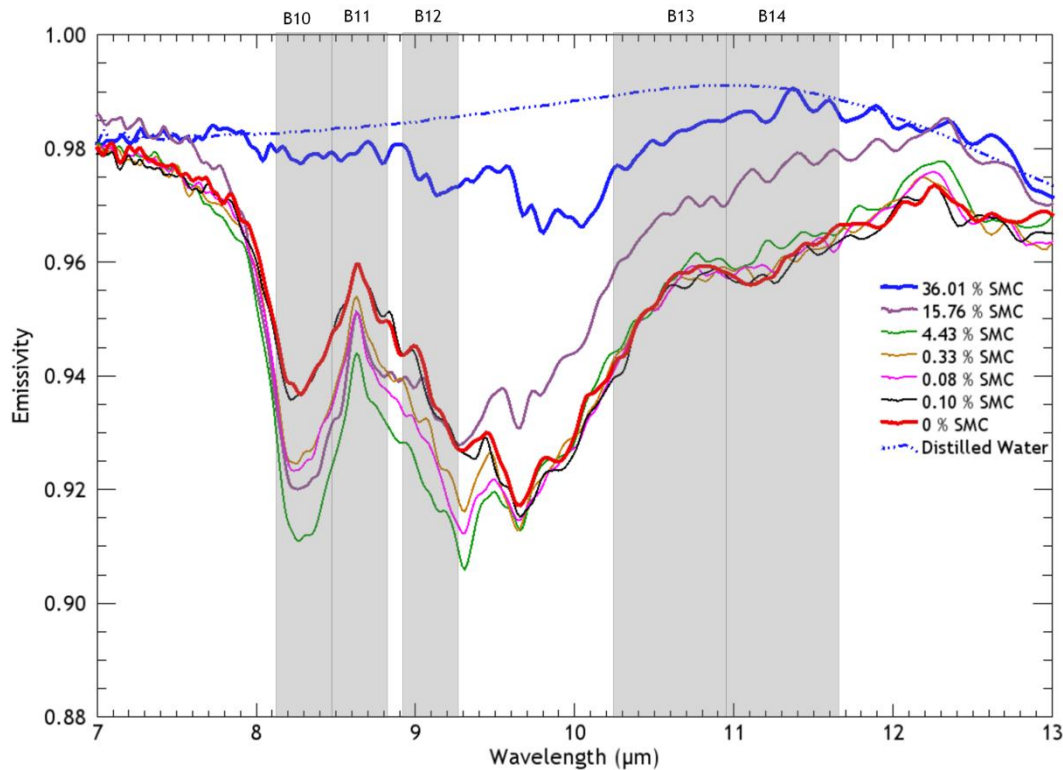
Figure 4 Loam soil emissivity measurements with changing SMC corresponding to Table 3. The horizontal axis is the wavelength in micrometers (μm) from 7 to 13 μm. The vertical axis is the emissivity with the maximum value of 1. The grey shaded regions are the position of the 5 ASTER TIR bands.

Lab measurements of saturated Loam showed less variation and higher emissivity values (0.97-0.98) than Sandy Loam (0.95-0.99) in the ASTER Wavelengths (8 - 12 μm). Even at dry state Loam emissivity values were higher (0.97) than Sandy Loam emissivity values (0.95-0.96) in B10 (8.2μm), B11 (8.6μm) and B12 (9μm) of ASTER for fully saturated states. Sandy Loam emissivity values in B13 (10.6μm) and B14 (11.3μm) were higher at 0.98-0.99 than Loam emissivity values (0.98) in the same bands for the wet conditions. Lowest emissivity values were observed in Sandy Loam for dry states in B10, B11 and B12 in the range 0.88-0.91 compared to Loam emissivity values (0.93-0.95) in the same bands. Emissivity value of 0.96 were found in Sandy Loam in B13 and B14 compared to Loam soil emissivity values of 0.95-0.96 in dry conditions.

Chapter 4 addresses the research objectives of soil moisture related anomaly detection by including the emissivity values of dry and wet soil in a Synthetic model. In order to test the anomaly detection rates extreme cases of dry and wet soils were chosen. For the wet conditions, Sandy Loam with 38% soil moisture content and Loam soil at 36% SMC were chosen as both the soils represent the highest soil moisture states. For the dry states 0% SMC was chosen for both soil types.

4. SYNTHETIC DATA MODELLING

The main aim of the synthetic data modelling analysis is to simulate the effects of soil moisture and anomaly size in detecting geothermal surface temperature anomalies. The purpose of creating a synthetic data model is two-fold. Firstly, to see how large a sub-pixel geothermal temperature component needs to be in order to be detectable as an anomaly. Secondly, to test various combinations of dry and wet conditions of soil covering the anomalous pixels and the background pixels. The model provides a framework to visualize the influence of soil moisture (emissivity variation) and its influence on the detectability of a thermal anomaly. The emissivity results of Chapter 3 are used in the synthetic model to answer the research objective of simulating the effects of soil moisture on geothermal anomaly detection. This chapter describes the methods and results of the synthetic data modelling analysis. The chapter is divided into three parts. Part A pertains to the core segment of the model and Part B is the extension to the model, both under the Methods. The Results section describes the outcome of the methods applied.

4.1. Methods: Part A

This section describes the steps for creation of the Core part of the synthetic model as illustrated in Figure 5. Since the thermal anomalies can be sub pixel in sizes therefore the pixel containing the anomaly is considered to be made of a background and hot spot geothermal temperature. Subsequently the fraction of the anomalous pixel is increased and the anomaly detection rates are checked.

The Synthetic Model (Figure 5) was created in ENVI IDL and the associated steps for the creation are described as follows:

1. Using the mean and standard deviation (Table 4) of typical background surface temperatures (Figure 7) present in geothermal areas of Yellowstone and Olkaria, a synthetic temperature Image (11 by 11) was created by selecting random temperature samples out of the population. For every iteration of the model a new random sample set is selected out of the same population to create a synthetic background temperature image.
2. The spectral radiance was calculated by applying the Planck function to the synthetic temperature in the wavelength range of 0.5 to 50μm multiplied with the emissivity. This resulted in a spectral radiance image.
3. The central pixel is assumed to be consisting of two sub-pixel components. A fraction with the anomalous thermal temperature and the rest of the pixel containing the background temperature component. Therefore, an In situ hot spot geothermal temperature was added to the central pixel which was used as a reference location for thermal anomaly detection. Again using the Planck function multiplied with the emissivity values the total Pixel Integrated Radiance Image was calculated. Pixel Integrated Radiance is the linear sum of radiance of the fractions contributed by the hot spot temperature and the background temperature.
4. Once the emitted radiance was calculated for the synthetic image, it was resampled to ASTER satellite wavelength ranging between 8 -12 μm using the ASTER TIR response functions(JPL, 2003).
5. Further, the temperature was estimated using the Emissivity Normalization tool in ENVI from the re-sampled ASTER wavelength. This resulting temperature is known as the Pixel Integrated Temperature (PIT). Emissivity Normalization is the process of estimating the temperature by fitting a black body curve onto the emissivity (Kealy & Hook, 1993).

6. The central pixel of the PIT synthetic image was used as an anomaly detection location. The central pixel was checked whether it had a temperature value greater than Mean + 2 Standard Deviation of the background values. For 1 hot spot temperature and 1 pixel fraction the anomaly detection process was iterated 100 times in order to check how many times the anomaly was detected. The only input parameters which change during the iteration process are the random sample of the background temperatures which is bound within the limits of the mean and standard deviation of the background temperature population. Thus, after 100 iterations if the anomaly was detected e.g., 6 times, the rate of success is simply calculated by taking the ratio of 6 by 100 which gives 0.06 as the anomaly detection rate. So for 1 pixel fraction and 1 hot spot temperature the result is a decimal number which ranges from 0 to 1 after running the model with 100 iterations.
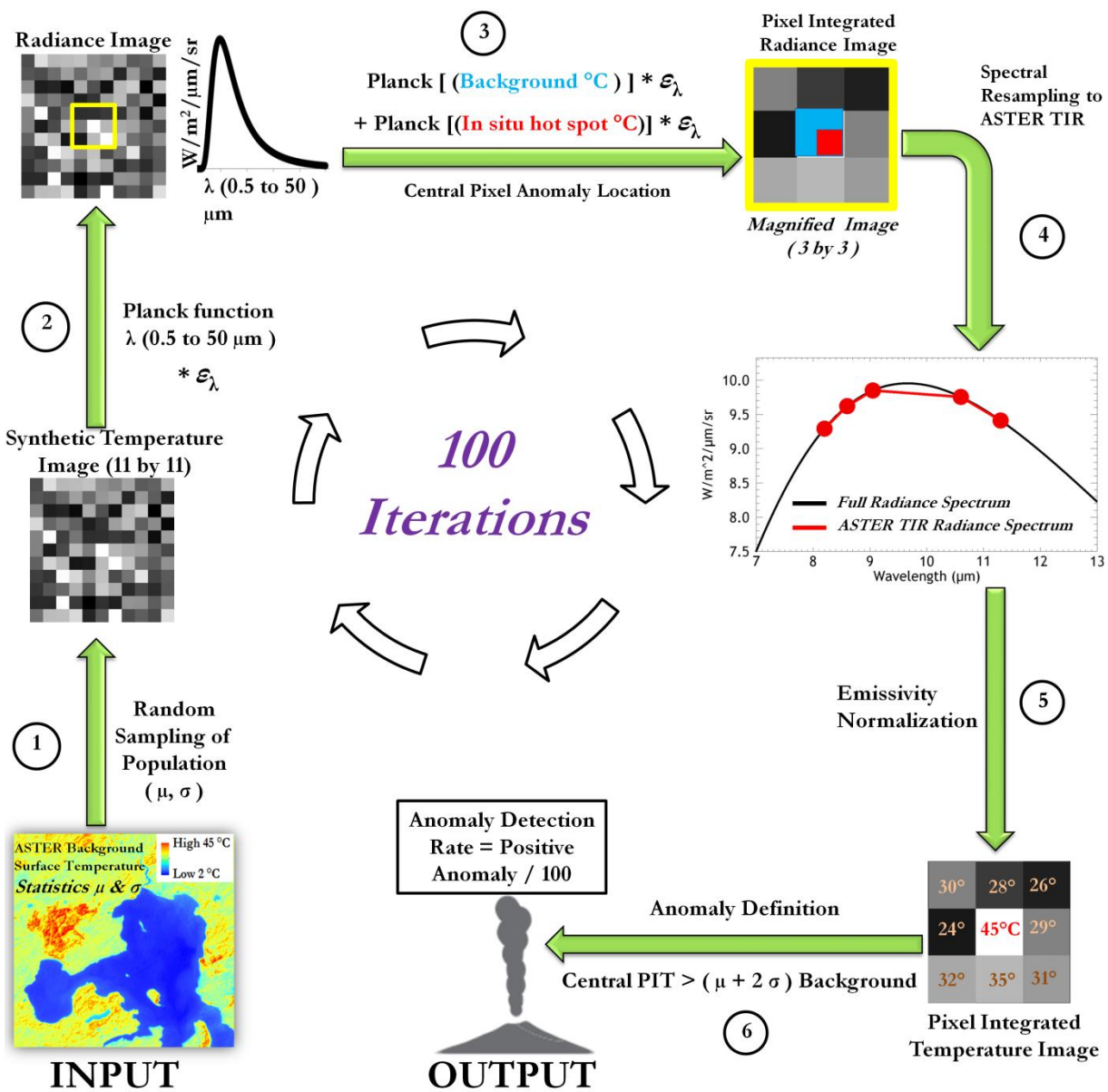
Figure 5 Work Flow showing the Core part of Synthetic Data Model: Part A

4.2.   Realistic Temperature Ranges

The input requirements for the synthetic model are background surface temperature statistics (mean and standard deviation), and In situ hot spot geothermal temperatures. Both background and in situ temperatures are retrieved from realistic temperature ranges.

Two geothermal areas, Yellowstone and Olkaria were chosen for this study because one area represents a higher latitude (44°N) and the other a lower latitude (°0) location on earth respectively. For Yellowstone, cloud free satellite surface temperature data were chosen between June-Sept 2012 to avoid the effects of insulation due to snow during the winter months. For Olkaria, months of January and February were chosen because the images were relatively cloud free during these months of 2012.

The background temperature statistics were collected from ASTER Surface Kinetic Temperature Satellite Image product (AST_08) because background temperatures vary gradually and satellite pixels of 90m can be used for this purpose. For the geothermal hotspot temperatures, ASTER data would not have been suitable since many data would be a mix of several surface temperatures at the ASTER pixel size. Instead, In situ hot spot temperatures were accessed from Yellowstone National Park Research Coordination Network from the Montana State University website (Sully et al., 2015) and the USGS Report (Bergfeld et al., 2011) for Yellowstone. Thermal temperatures ranged from 13°C to 94°C. Similarly, for retrieving geothermal hot spot temperatures for Olkaria, Geothermal Activity Map of Kenya was used (Ledgard, 1989). Temperatures ranged from around 30°C to 94°C. In situ hot spot temperatures are point measurements of temperatures collected from thermal areas on the ground.

Both Day and Night ASTER Satellite temperature images from the same geothermal location were layer stacked together. This was useful in order to extract the statistics out of the same background area for all day and night temperature images for different dates. For Night time temperature images there was a need for geo-adjustment for correct alignment with Day time temperature images. The geo adjustment method followed by Vaughan et al. (2012) was used here for adjusting the night time ASTER images. The background areas were digitized using the 'region of interest (ROI)' tool in ENVI. The process of defining a background region was based on visual inspection of ASTER Images, Google Earth Pro images and ancillary information associated with the area. First of all known thermal areas in Yellowstone and Olkaria were overlaid on ASTER Images. The area immediately surrounding the vicinity of thermal area was delineated in ASTER Images. The size of the background surfaces which were digitzed were considerably large compared to the thermal areas. Large background areas were digitized in order to extract a wide range of background temperatures covering different land covers surrounding the thermal area.

4.3. Methods: Part B

Figure 6 shows extension to the core model created in Part A. The added components are the dry and wet soil emissivity measurements from Chapter 3 which can be used either with the background pixels in the 11 by 11 synthetic image or it can be used with the anomalous pixels or both simultaneously. Further, the pixel fraction is also varied from 0 to 1 for the anomalous temperature. In addition, 10 hot spot temperatures are included in the model to test the anomaly detection on geothermal temperatures of Yellowstone and Olkaria ranging from 10°C to 94 °C. The 100 iteration procedure applied in Part A with 1 hot spot temperature, 1 pixel fraction is now extended to 10 hot spot temperatures, 12 pixel fractions and different soil emissivities.
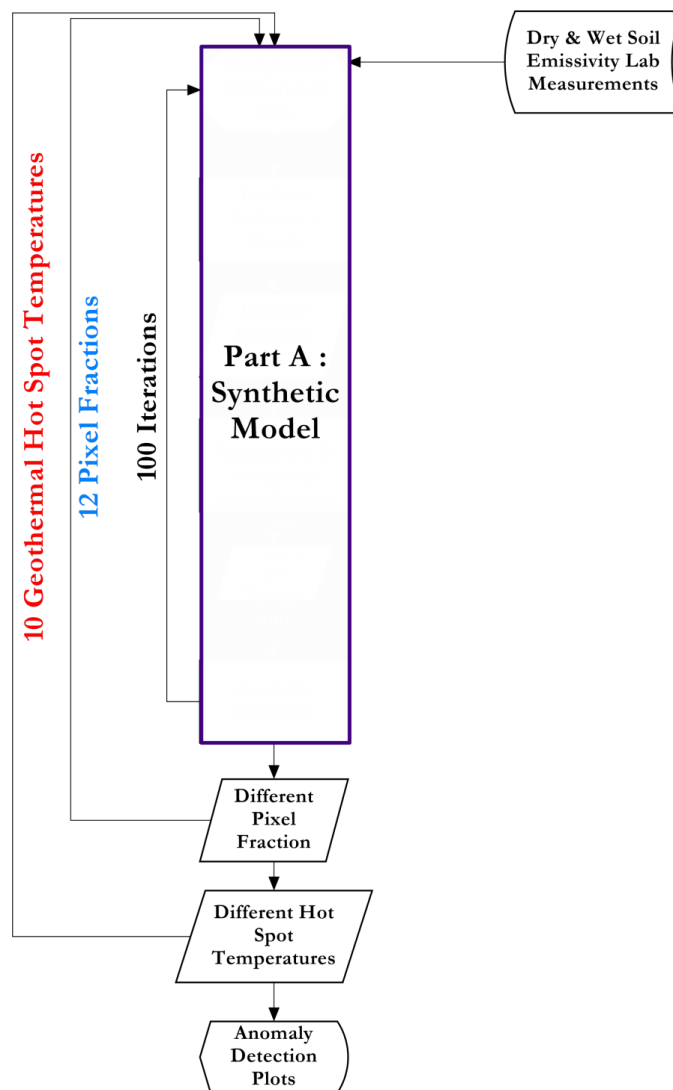
Figure 6 Extension to the Synthetic Model: Part B

The emissivity values of dry and wet soils can be used either with the 11 by 11 background image, or in the background of the central pixel or with the hot spot temperature in the central pixel. The emissivity values in this study were used in all the three locations of the synthetic image with various combinations of dry or wet soil generating 16 possible combinations. These combinations are presented in Table 5.

4.4.   Results

The result section is divided into five sub sections. The first section shows the background temperature statistics and spatial results. The second section illustrates how to read the plots generated from the synthetic data model. The third section is about the differences in day and night scenarios obtained by the synthetic data model. The fourth section describes sixteen dry and wet soil combinations of anomaly detection scenarios generated from the synthetic data model. The fifth section ends with the effect of sensor noise on anomaly detection

4.4.1.   Background Temperature Statistics & Spatial Results

Figure 7 A & B show the spatial results of the background areas which were digitized in ASTER satellite temperature data product (AST_08) for two different geothermal locations, Yellowstone, US and Olkaria in Kenya. The shape files of the background regions shown in brown color are overlaid on Google Earth Pro Images.The thermal areas are seen in yellow color in both the images.In addition the day and night common boundary of ASTER Images are also displayed with a black outline. The green line represents the Park boundary of Yellowstone and Olkaria Volcanic Complex. The background can be clearly seen as covering relatively larger area compared to the thermal areas. Moreover, the thermal areas shown in yellow are actually magnified three times their actual size for clarity at the scale of the image.

The results of the background temperature statistics collected for Yellowstone and Olkaria are summarized in Table 4. The mean background surface temperatures in Yellowstone extracted from three night time images were found to be 9°C and 29°C for day time images with a standard deviation of 1.89°C and 4.72°C respectively. Similarly, for Olkaria the mean background surface temperatures were found to be 10°C for three night times images and 36°C for two day time images with a standard deviation of 2.61°C and 4.03°C. Clearly, the day time background temperatures have higher mean background temepratures and standard deviation compared to the night time statistics.

Table 4 Background Temperature Statistics Summary. Location column shows the geothermal area, YNP stands for Yellowstone. The Date column shows the dates of image acquistion. Background temperature mean µ column shows the mean background temperature for the corresponding row of day and night for a particular area. Like wise the standard deviation of the background temperature is in the last column.

Location, SCENARIO	Date (2012)			Background Temperature Mean (µ)	Background Temperature Standard Deviation (σ)
YNP, Night Time	12th July	27th July	28th August	9 °C	1.89°C
YNP, Day Time	30th June	17th August	18th September	29°C	4.72°C
Olkaria, Night Time	7th January	23rd January	24th February	10°C	2.61°C
Olkaria, Day Time	12th January	22nd February	--	36°C	4.03°C
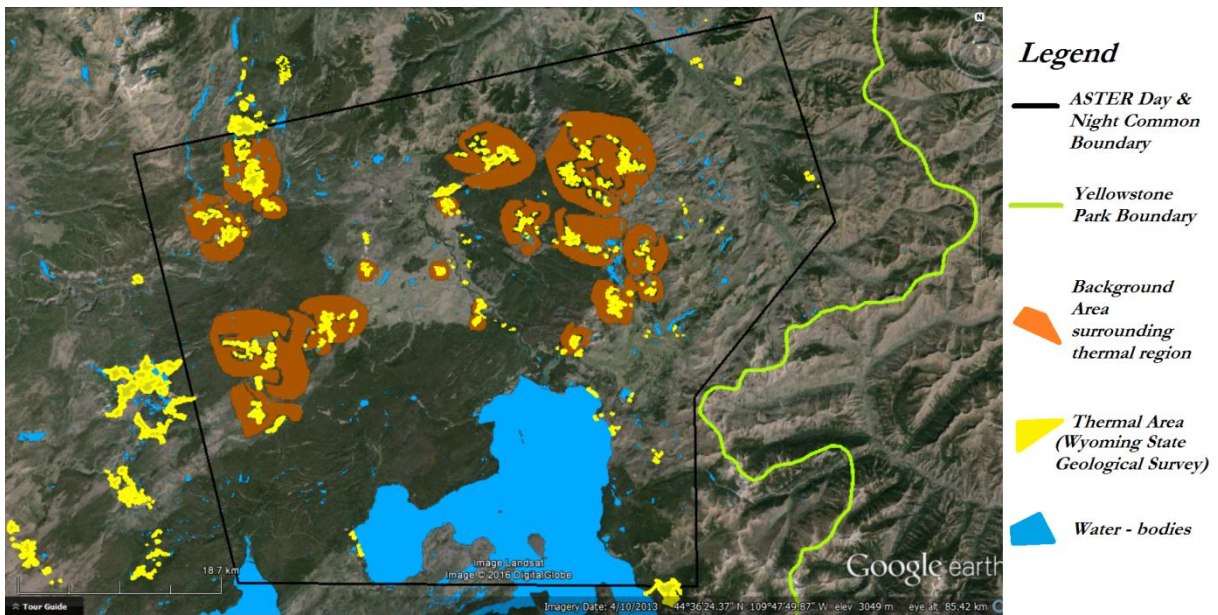
A.
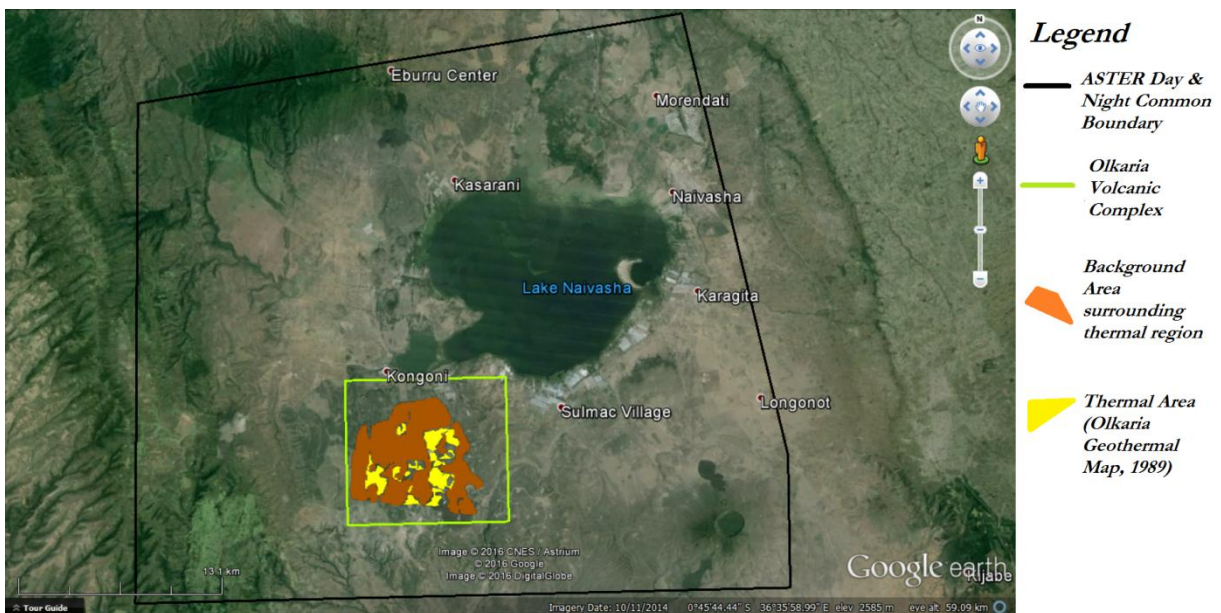
B.

Figure 7 Background Area surrounding thermal region overlaid on Google Earth Pro Images. A shows the background regions digitized over Yellowstone. B shows the background area within Olkaria Volcanic Complex south of Lake Naivasha.

4.4.2.   Synthetic Data Modelling Results – Understanding & Interpretation of Results

Figure 8 shows the matrix plots generated from the synthetic data model beginning from the simplest case i to a complete matrix plot case shown in iv. All the four plots have the same background temperature statistics of night time Yellowstone scenario of mean Tbg μ =9 °C and std.dv Tbg σ =1.89°C. The results can be read as follows:

i.   When the anomalous temperature represented by the hot spot temperature of 10 °C covers 0 part of the pixel, the anomaly detection rate is represented by the dark red coloured square. Here the background temperature statistics are mean Tbg μ =9 °C and std.dv Tbg σ =1.89°C. Dark red colour shows that the detection rate is almost 0 (Color scale bar in Figure 8 iv). The result was generated after running the synthetic model for 100 iterations with 0 pixel fraction when the hot spot temperature is 10°C. The ratio of the number of times the anomaly was detected to the total number of iteration gives the detection rate. The detection rate is low when the anomalous temperature is close to the background temperature statistics.

ii.   Further, when the anomalous temperature represented by hot spot temperature of 10°C covers 0 part to 1(completely covered) part of the pixel, the detection rates are displayed as a single row of coloured squares for each pixel fraction. In this example (Figure 8 ii) the dark red color shows that detection rates of still close to 0. Detection rate associated with each pixel fraction was generated after running the model for 100 iterations each. Even when the pixel is completely covered by the anomalous temperature (at 1 pixel fraction), the anomaly detection rates are low because the anomalous pixel temperature does not rise above the μ + 2σ of the background criteria for the anomaly to be detected.

iii.   The plot shown in Figure 8 iii. shows two rows of detection rates for two different hot spot temperatures namely 10°C and 20 °C respectively. The detection rates drastically improve after the anomalous temperature represented by 20°C covers 30% to 50% of the pixel. The area is highlighted with a black dashed outline showing light brown to dark green coloured squares with detection rates from 0.3 to 1 respectively.

iv.   The full fledged graphical matrix plot in Figure 8 iv. shows a complete set of anomaly detection rates when the hot spot temperatures range from 10°C to 94°C covering the full range of geothermal hot spot sub pixel temperatures in Yellowstone. Each horizontal row represents detection rates for one hot spot temperature with 12 pixel fractions ranging from 0, 0.05, 0.1, 0.2, and so on until 1. The background temperature statistics are the same as in i. Overall it can be seen that as the temperature and size of the hotspot increases, the anomaly detection rates also increase.

10 °C

0

Pixel Fraction

i.

ii.

iii.

iv.
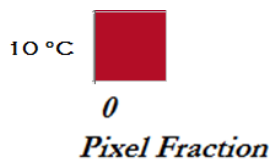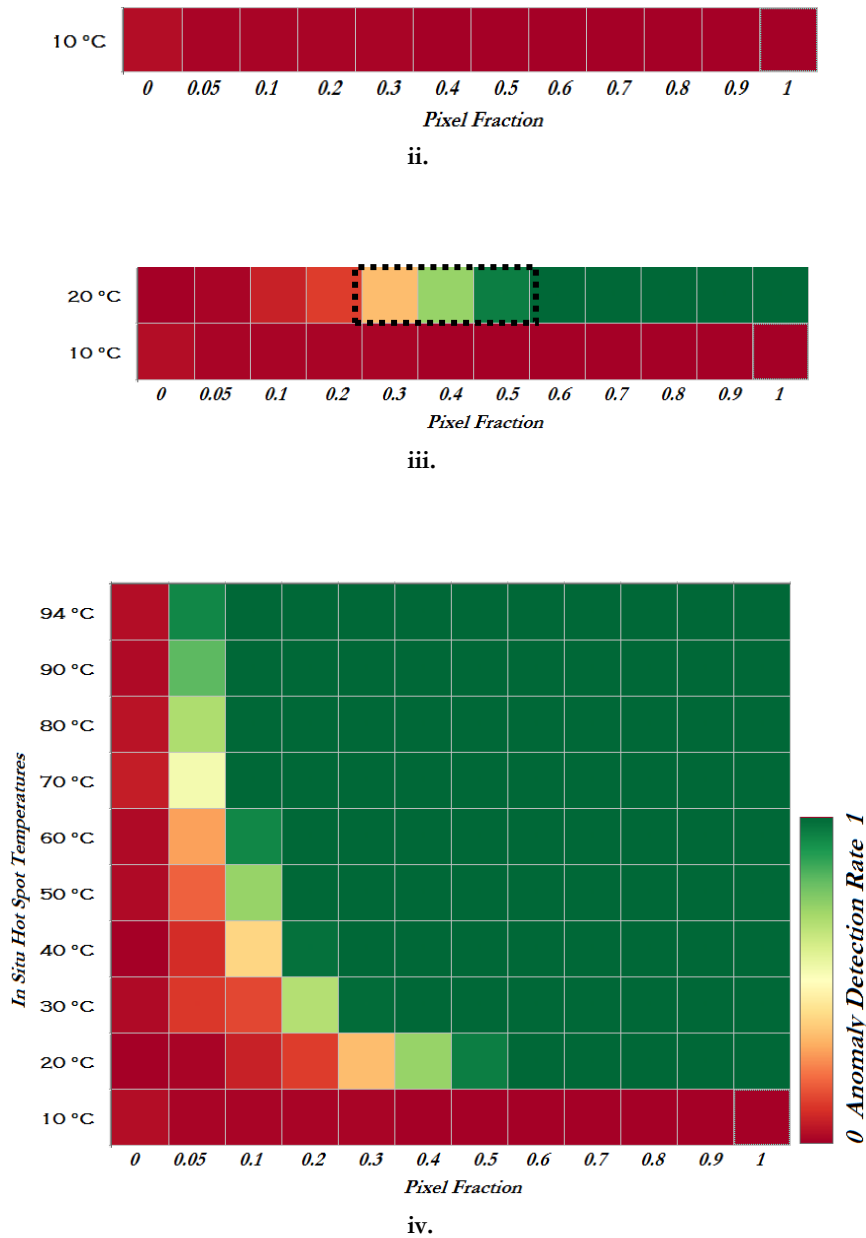
Figure 8 Simple to complete matrix plots generated from the Synthetic Model. From i. to iv. The background temperature statistics are the same, i.e., Tbg µ = 9°C, Tbg σ = 1.89°C. The horizontal axis shows the pixel fractions and the vertical axis shows the in situ hot spot temperatures. The colour bar shows the detection rates beginning at 0 which is dark read to dark green colour at 1.

4.4.3.   Synthetic Data Modelling Results – Differences between Day and Night

In order to see the differences between day and night through the synthetic data modelling analysis, Yellowstone and Olkaria background temperature statistics and in situ hot spot temperature ranges for the respective areas were used. Tbg µ mean background surface temperature and Tbg σ standard deviation values for Yellowstone and Olkaria were taken from Table 4.

The differences between day and night in anomaly detection is very clear from the two plots (Figure 9, ii, iv) of night time scenarios in Yellowstone and Olkaria with overall mean detection rates of 0.741 and 0.81.

However, the mean detection rates of Yellowstone include 10 hot spot geothermal temperatures and for Olkaria there are 8 hot spot temperatures. Therefore, in order to compare both, Yellowstone mean detection rate with 8 hot spot temperature has to be included which comes out to be 0.85. The overall mean detection rates in Yellowstone (0.85) are higher as compared to Olkaria (0.81) for night time scenarios. Yellowstone and Olkaria represent two different climatic and geological settings. Yellowstone belongs to a more temperate kind of climate and Olkaria fits more towards the tropical kind of climate. Olkaria is also on a higher elevation but not as high as Yellowstone. From the synthetic data plots in Figure 9 (ii and iv) and Table 4 it can be seen that the background temperature standard deviation of night time Olkaria is higher at 2.61°C compared to Yellowstone background temperature standard deviation of 1.89°C. The differences in standard deviations of background temperatures show that there might be variations due to climatic and geographic locations in both the areas.

The day time scenarios have an overall mean detection rate of 0.438 and 0.507 (Figure 9, i, iii). However when the Yellowstone area is compared with Olkaria for 8 hot spot temperatures common to both it is found that the Yellowstone overall mean detection rates are better with a value of 0.54. The better detection rates in night time scenarios are represented by more number of dark green squares covering the plots as compared to day time scenario.
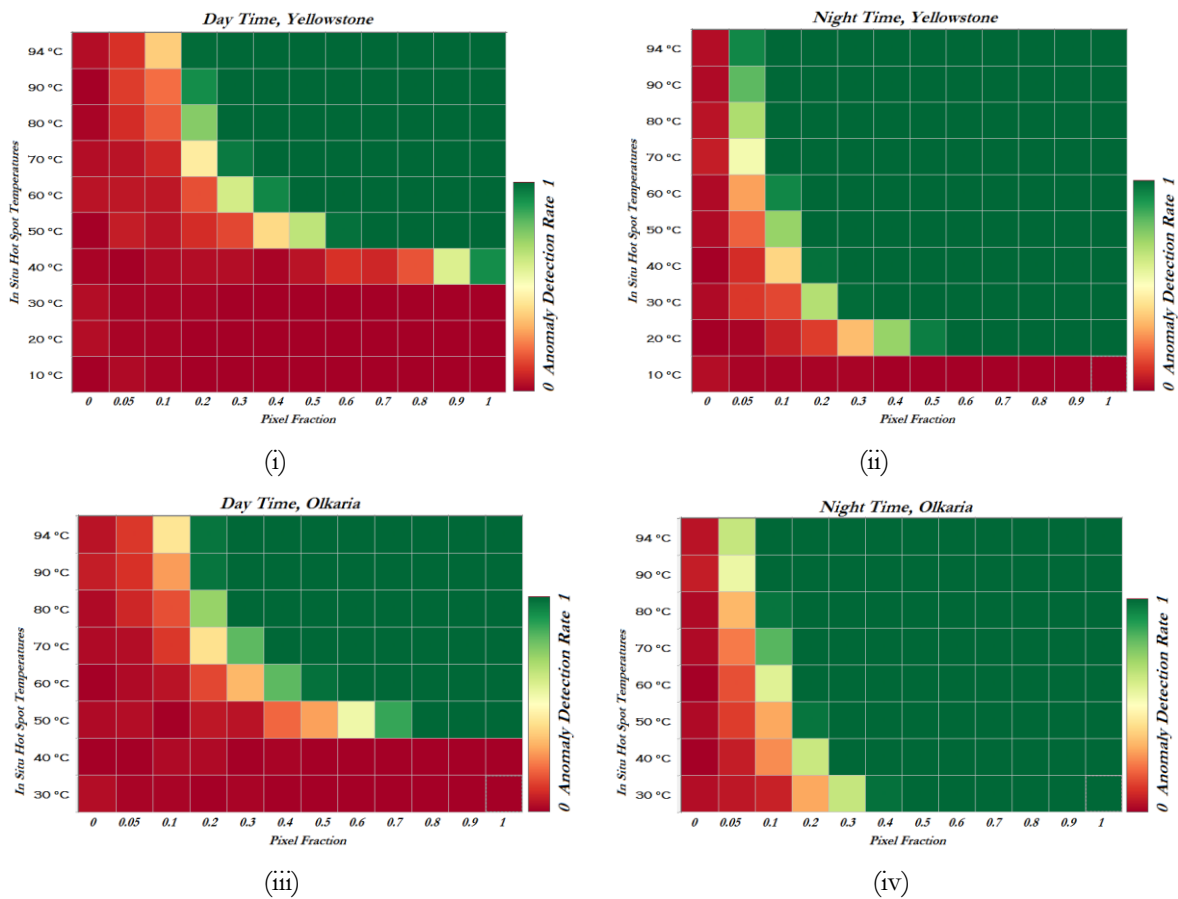
Figure 9 Day and Night Differences in Anomaly Detection. The horizontal axis consists of pixel fractions ranging from 0 to 1. The vertical axis consists of In situ Hot Spot temperatures ranging from 10 °C until 94 °C stacked one above the other row wise for Yellowstone (i & ii) and 30°C to 94°C for Olkaria (iii & iv). The colour bar on the right shows the anomaly detection rate from 0 to 1. Overall Mean Detection Rate are (i) 0.438,0.54 (ii) 0.740 (iii) 0.507 (iv) 0.81

4.4.4. Synthetic Data Modelling Results – Combinations of Dry & Wet Soil Emissivity variation

The results in this section describe the outputs generated from the synthetic model by taking into account the emissivity of dry and wet loam and sandy loam soils from Chapter 3. Dry and wet soil emissivity can be used either with the background pixels or the anomalous pixels or both the pixels together in order to see their influence on thermal anomaly detection. With two different kinds of soils and two different conditions of wet and dry there are all together 16 combinations possible when allocating the dry and wet soils to the background and anomalous pixels. From the previous section it was found out that night time scenarios are better suited for anomaly detection. Therefore for testing the emissivity variations due to soil moisture night time Yellowstone setting was chosen to test all sixteen combinations. The results of the 16 combinations are presented in Figure 11 and corresponding Table 5. The serial numbers of the combinations in Table 5 correspond to the anomaly detection plots in Figure 11.

Table 5 Anomaly Detection Summary for 16 scenarios. The first column of Sr. No. corresponds to the numbers of Anomaly detection matrix plots from Figure 8. The second column shows the emissivity of dry or wet soils covering the background pixels. The third column shows similarly the emissivity of dry and wet soils covered by the anomalous pixels. Overall mean detection rate and standard deviation are present in fourth and fifth table column.

Sr.No.	Background Pixels	Anomalous Pixel	Overall Mean Detection Rate	Std. Dv.
i (A)	Wet Loam	Wet Loam	0.742	0.407
i (B)	Dry Loam	Dry Loam	0.741	0.408
ii (A)	Wet Sandy Loam	Wet Sandy Loam	0.74	0.408
ii (B)	Dry Sandy Loam	Dry Sandy Loam	0.74	0.408
iii (A)	Dry Loam	Wet Loam	0.752	0.403
iii (B)	Wet Loam	Dry Loam	0.73	0.413
iv (A)	Dry Sandy Loam	Wet Sandy Loam	0.748	0.404
iv (B)	Wet Sandy Loam	Dry Sandy Loam	0.732	0.411
v (A)	Dry Loam	Wet Sandy Loam	0.751	0.402
v (B)	Wet Sandy Loam	Dry Loam	0.728	0.412
vi (A)	Dry Sandy Loam	Wet Loam	0.747	0.404
vi (B)	Wet Loam	Dry Sandy Loam	0.733	0.41
vii (A)	Dry Loam	Dry Sandy Loam	0.745	0.405
vii (B)	Dry Sandy Loam	Dry Loam	0.737	0.409
viii (A)	Wet Loam	Wet Sandy Loam	0.742	0.406
viii (B)	Wet Sandy Loam	Wet Loam	0.741	0.407

i(A)   i(B)

ii(A)

ii(B)

iii (A)

iii (B)

iv (A)

iv (B)

v (A)

v (B)

vi (A)

vi (B)

vii (A)

vii (B)

viii (A)
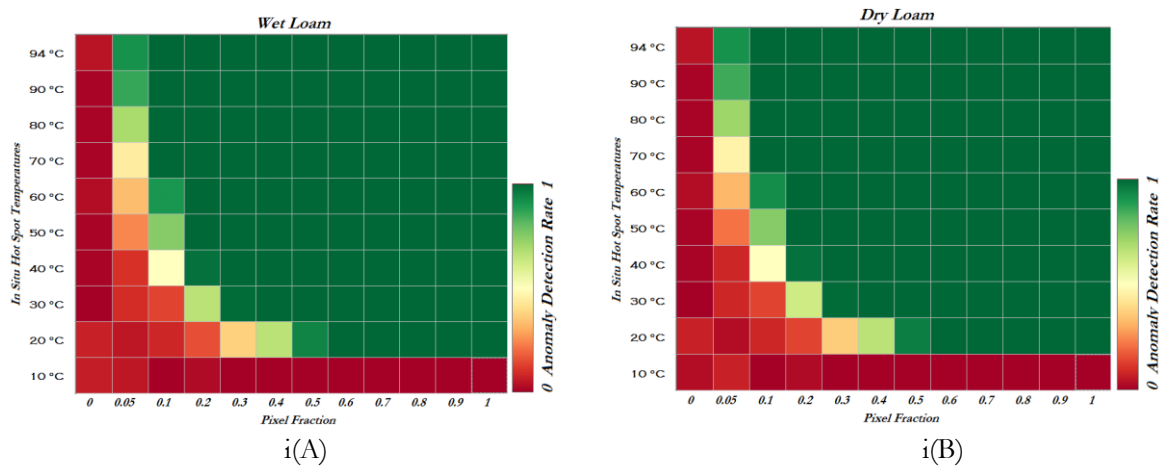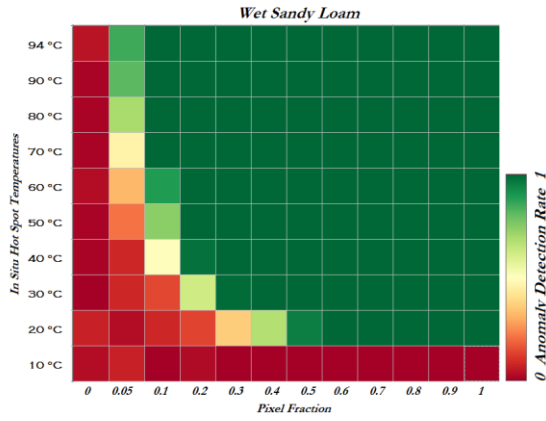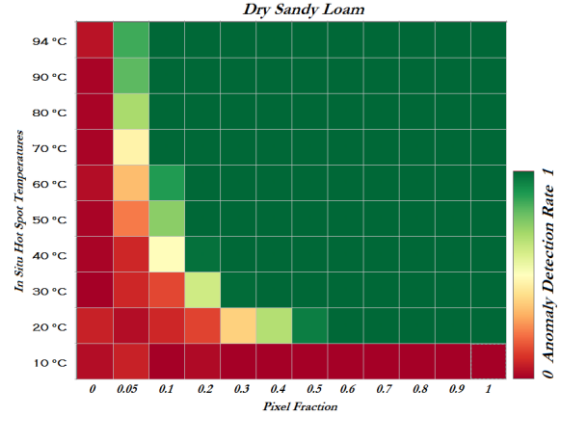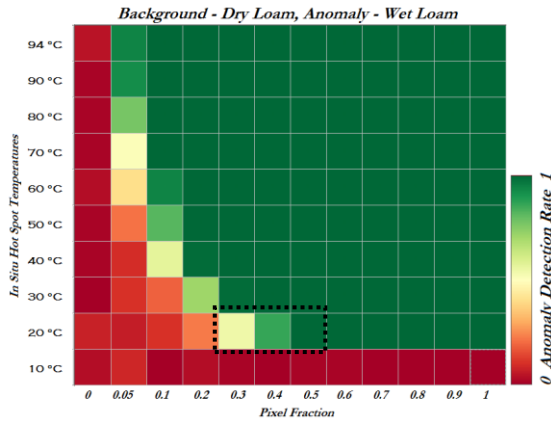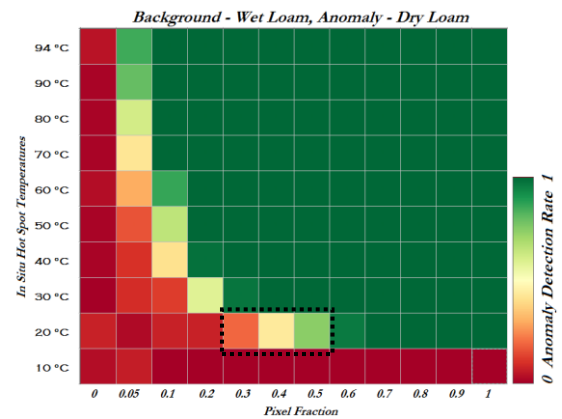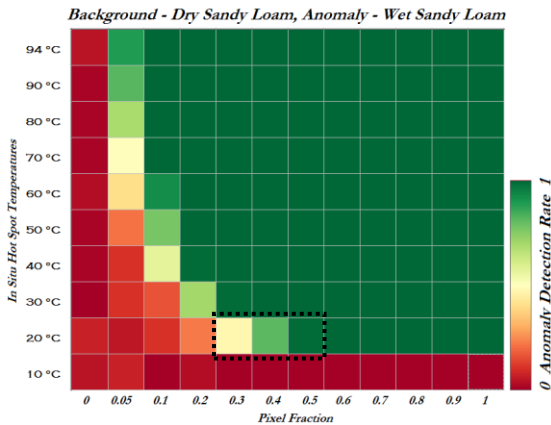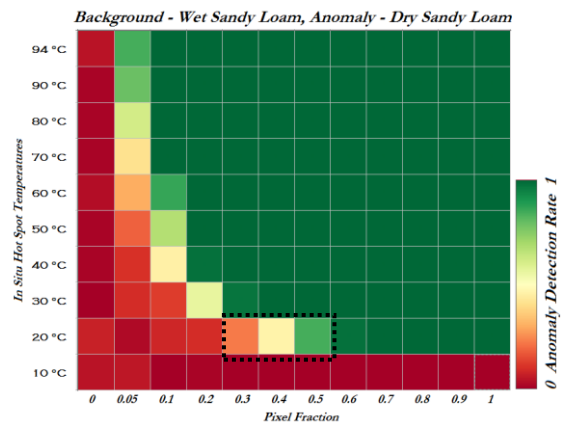
viii (B)
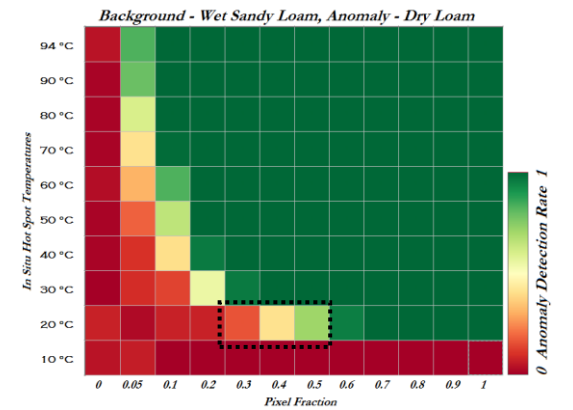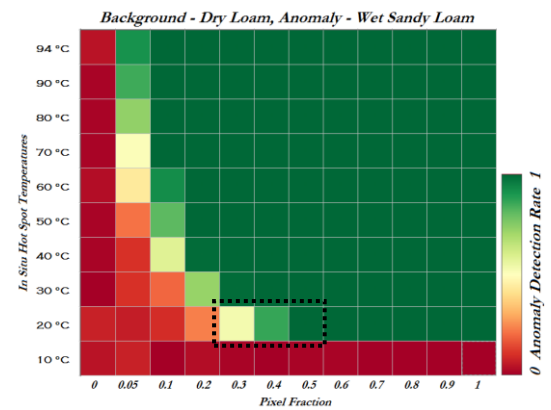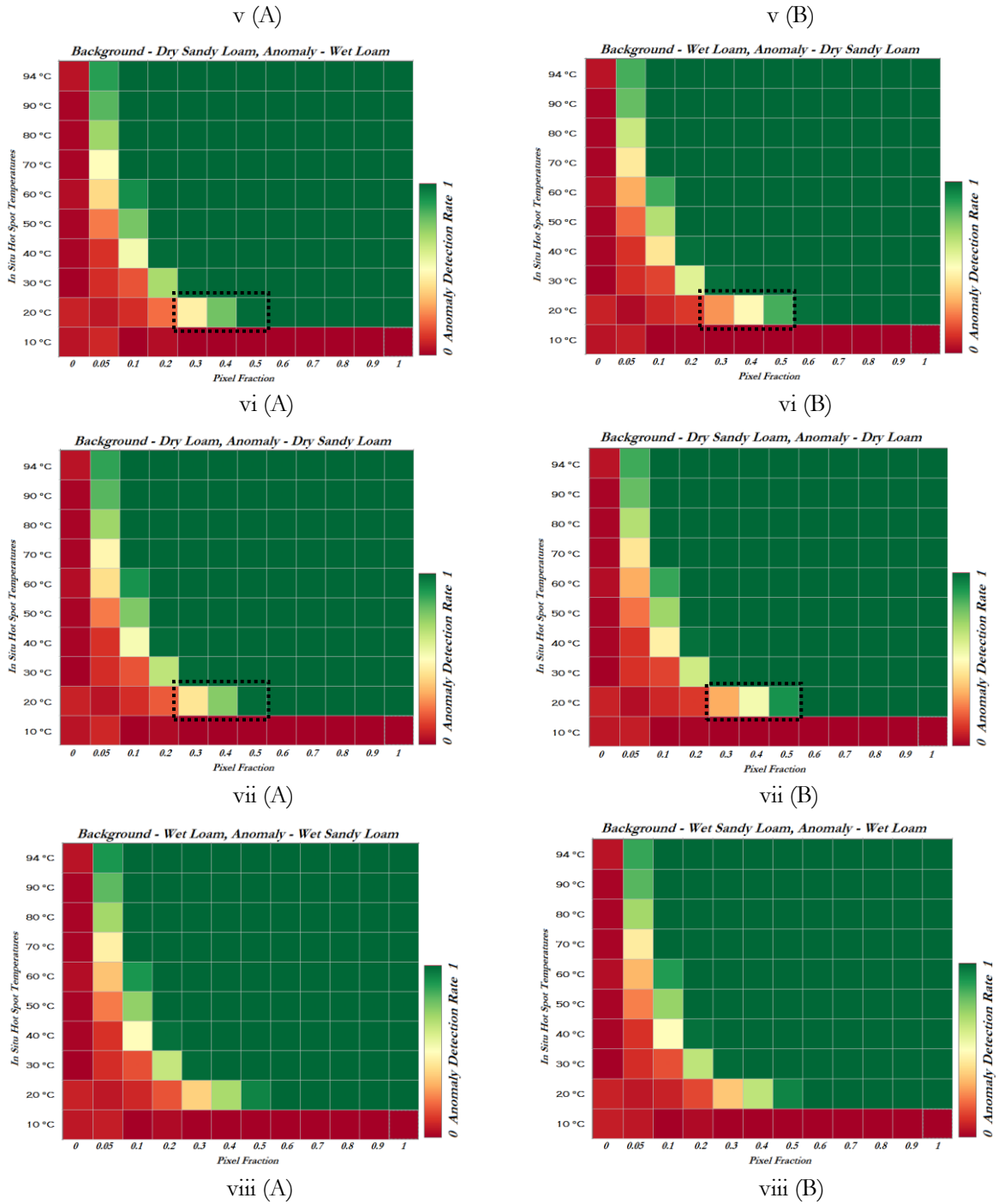
Figure 10 Anomaly Detection Plots associated with Table 5. The background temperature statistics are the same for all the plots Tbg μ = 9°C, Tbg σ = 1.89°C and they represent Yellowstone night time background temperature statistics.

For easy interpretation a dotted box is added from iii (A) to vii (B) anomaly detection plots over 0.3 to 0.5 pixel fractions corresponding to 20°C hot spot temperature where the changes in detection rates can be clearly differentiated. Overall the detection plots show a pattern beginning with low detection rates corresponding to lower hot spot temperatures such as 10°C. The lowest detection rates are associated with dark red colour and the highest detection rates are represented by dark green colour. The colour patterns

in detection rate changes more towards dark green colours with the increase in hot spot temperatures and pixel fractions.

Figure 10 i(A), i(B) and ii(A), ii(B) Plots show fully saturated and completely dry Anomaly Detection matrix plots for Night time scenario in Yellowstone of Loam and Sandy Loam Soils respectively. The differences between Plot i(A) and i(B) in Loam Soils' case are minute (From Table 5. i(A) and i(B) mean detection rates of 0.742 and 0.741 for fully saturated and dry loam soil respectively). In the Sandy Loam soils' case ii(A) and ii(B) there is no difference between the mean anomaly detection rates when the pixels are covered with fully saturated and when the pixels are covered with completely dry sandy loam soil (From Table 5. ii(A) and ii(B) mean detection rates are the same 0.74 for fully saturated and dry sandy loam soil). There are no differences in detection rates with neither soil type nor soil moisture conditions of soils as long as the central anomalous pixel is the same as surrounding background pixels (Figure 10 i & ii).

If the central anomalous pixel is wet and the surrounding is dry, the detection rate goes up. The soil type seems to be of little influence (Figure 10 iii(A), 11 iv(A), v(A), vi(A)). Figure 10 iii(A) shows when the background pixels are covered with dry loam and the anomalous pixel is covered with fully saturated loam the overall mean detection rate is 0.752 which is better compared to when the situation is reversed (From Table 5. iii(A) and iii(B) mean detection rates of 0.752 and 0.73 respectively)In the case of Sandy Loam Soils' from Figure 10 iv(A) and iv(B) scenario it can be seen that the detection rates are better when the anomalous pixel is covered with fully saturated sandy loam soil and the background is covered with dry sandy loam (From Table 5. iv(A) and iv(B) mean detection rates of 0.748 and 0.732 respectively). From Figure 10 v(A) when the anomalous pixel is covered by fully saturated Sandy Loam and the background pixels are covered by dry loam soil the detection rates are better than when the conditions are reversed in v(B) (From Table 5. v(A) and v(B) mean detection rates of 0.751 and 0.728 respectively). Similarly, in Figure 10 vi (A), when the anomalous pixel is covered by wet loam and the background is covered by dry Sandy Loam the detection rates are better than when the conditions are reversed in vi(B) (From Table 5. vi(A) and vi(B) mean detection rates of 0.747 and 0.733 respectively).

When the central anomalous pixel is dry and the surrounding background region is wet, then the detection rates is going down as compared to all the same emissivity (Figure 10 iii(B) and iv(B)

From Figure 10 vii(A), when the anomalous pixel is covered by dry Sandy Loam and the background pixels are covered by dry Loam Soil the detection rates are better than when the conditions are reversed in vii(B) (From Table 5. vii(A) and vii(B) mean detection rates of 0.745 and 0.737 respectively). From Figure 10 viii(A), when the anomalous pixel is covered by fully saturated Sandy Loam and the background pixels are covered by fully saturated Loam Soil the detection rates are almost similar when the conditions are reversed in viii(B) (From Table 5. viii(A) and viii(B) mean detection rates of 0.742 and 0.741 respectively).

Out of all the detection plots in Figure 10 and Table 5, the best anomaly detection rates are achieved in iii(A), iv(A), v(A) and vi(A) when the Anomalous pixel is covered by wet soils and the background pixels are covered by dry soils. And the worst detection rates are observed in iii(B), iv(B), v(B) and vi(B) when the anomalous central pixel is covered by dry soils and the background is covered by wet soils.

4.4.5.   Synthetic Data Modelling Results – Sensor Noise Effects

The effect of ASTER TIR Subsystem sensor noise for all 5 TIR Bands are represented by the NEdT value which is ≤0.3 °K (Gillespie et al., 1998). Therefore to test the differences in anomaly detection between two scenarios, one without and one with sensor noise, Night Time Yellowstone setting was chosen. Figure 11, A and B show two anomaly detection plots with and without sensors noise effects for night time Yellowstone setting. The overall mean detection rate of the plot without sensor noise added to the anomaly detection was found to be 0.740 and when the sensor noise is added to the anomaly detection, the value showed 0.732. There is a difference in 0.08 in the overall detection rate when 0.3 °K is added to the anomaly definition of $\mu + 2\sigma + 0.3$ compared to without the addition of the NEdT value. The differences are insignificant. The NEdT is the Noise Equivalent difference in temperature of the ASTER TIR subsystem. In practical terms it means that ASTER TIR cannot detect temperature differences of less than 0.3°K at the reference temperature of 370°K. In the context of thermal anomaly detection it means that the temperature differences between the anomalous pixels and the background pixels must be greater than 0.3°K in order for ASTER TIR to detect the anomaly. Usually the temperature differences between the anomalous area and the background area are easily greater than 0.3°K, therefore NEdT value does not have a major effect on the anomaly detection rates which is also shown graphically by Figure 11 and by the small difference in overall mean detection rates.

A.   B.
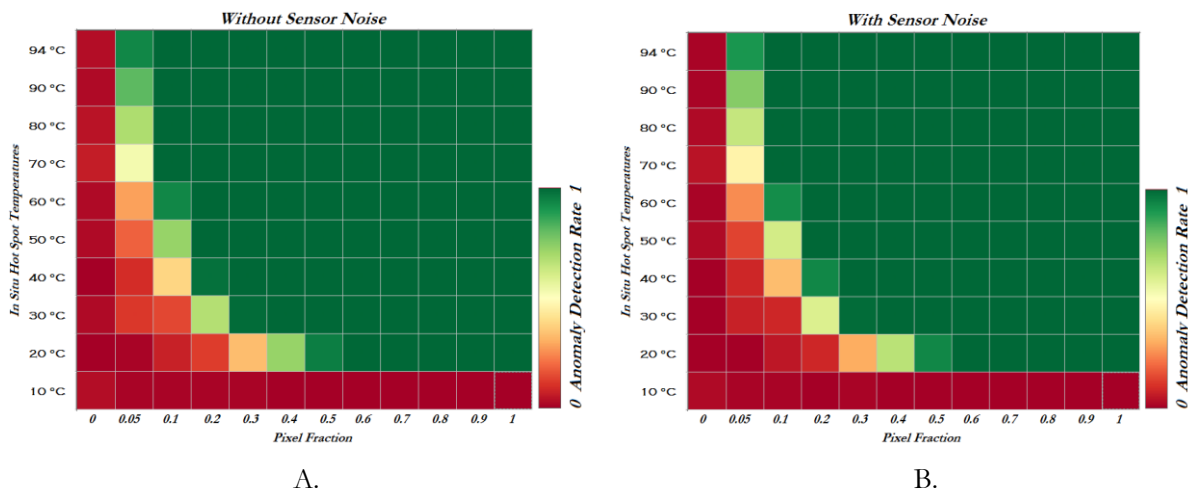
Figure 11. Sensor Noise Effects on Anomaly Detection. The setting is Night time in Yellowstone. Tbg μ stands for mean background surface temperature, Tbg σ stands for background standard deviation. The horizontal axis consists of the pixel fractions ranging from 0 to 1. The vertical axis represents In situ Hot Spot temperatures ranging from 10 °C until 94 °C stacked one above the other row wise. The colour scale bar on the right shows the anomaly detection rate from 0 to 1. The lowest detection rates (closer to 0) corresponds to dark red colour with the highest detection rates of 1 in dark green colour. (i) has an overall mean detection rate of 0.740 and (ii) has 0.732.

5.   REMOTE SENSING TIME SERIES DATA ANALYSIS

This chapter addresses the third research objective from section 1.4.1 which is to analyse remote sensing datasets to examine the effects of soil moisture in detecting geothermal surface temperature anomalies. By analysing ASTER surface temperature, emissivity and emitted radiance images the influence of soil moisture on thermal anomalies is examined. The methods of the time series data analysis are described in section 5.1 followed by the results in section 5.2.

5.1.   Methods

The aim of this section is to analyse real remote sensing data for soil moisture related surface temperature anomalies for a thermal area in Yellowstone. Parameters that are assessed include Surface Temperature, Emissivity and Surface Emitted TIR Radiance data in relation to Precipitation and Soil Moisture data.

Criteria for Data Collection

In order to assess the surface temperature, emissivity, surface emitted TIR radiance in remotely sensed satellite images, ASTER satellite was chosen because it provided the best spectral (5 TIR bands), spatial (90m) and temporal (16 days) coverage. However, there is limited number of cloud free satellite images immediately after a precipitation event. It is rare to find day and night time ASTER image pairs for the same day for thermal inertia mapping. Therefore, the first requirement was to find cloud free, day and night images from summer time in Yellowstone. Summer time in Yellowstone is accompanied by thunderstorms in the afternoon. Winter time was avoided because of insulation effects due to snow. After searching the ASTER Images' database from NASA Earth Science Data Search webpage, June to September 2012 summer months provided the best match for the study with relatively cloud free images.

Remotely sensed soil moisture data is available from multiple satellites. SMAP satellite has the highest spatial resolution of soil moisture data of 3 /9/ 36 km and covers the time period from mid April 2015 until 7th July 2015 with ongoing acquisitions. In this time period only 2 ASTER scenes were available for Yellowstone with 99 percent cloud cover and 6 percent cloud cover respectively, which are few to analyse in this study. Out of the other soil moisture retrieving satellites SMOS (30-50 km), ERS 1/2 Scatterometers (25)/ 50 km), and ASCAT (25 km with grid spacing of 12.5 km), ASCAT provided the best coverage and spatial resolutions. The relative surface soil moisture data from ASCAT Metop satellite has a frequency of 1-2 days with some occasional data gaps. Therefore, to assess the soil moisture states of the ASTER Images, relative surface soil moisture from the same time period (June to September 2012) and from the same location were collected from ASCAT Metop satellite to relate to the ASTER Images. Precipitation data was collected from NOAA data that are daily summaries at the end of the day for the same time period from June to September 2012 in order to see how it relates to soil moisture data from ASCAT. The sources of Precipitation and Soil Moisture data are provided in Table 1. The acquisition time of ASTER scenes and acquisition time of Soil Moisture measuring ASCAT Metop satellite has some hours (>5hrs) of difference. Ideally it would be worthwhile to have an ASTER Image taken exactly at the moment when ASCAT Metop acquires Soil Moisture information. But this is not realistic as both the satellites have different orbit times. Nevertheless, it was decided to analyse the existing data that were available for possible correlation.

Table 6 shows the summary of the remote sensing data collected for the time series data analysis. This table includes 4 Night time and 3 day time ASTER Images of Surface Temperature, Emissivity and Surface Radiance TIR that were collected. Day Time images of ASTER are acquired around 12:30 hrs noon and Night time ASTER Images are acquired around 23:30 hrs over Yellowstone. Precipitation and Relative soil moisture data summary from NOAA and ASCAT Metop are also included for the time period between June and September 2012. GIS data (shape file) of a thermal area known as Sulfur Hills in Yellowstone was used as the reference location for the remote sensing time series data analysis.

Table 6 Summary of Data used in the Time Series Data Analysis

Data Type	Data Code	Time Period	Number of Images
ASTER Surface Kinetic Temperature	AST_08	June 2012 - Sept 2012	4 Nights, 3 Days
ASTER Emissivity	AST_05	June 2012 - Sept 2012	4 Nights, 3 Days
ASTER Surface Radiance TIR	AST_09T	June 2012 - Sept 2012	4 Nights, 3 Days
Precipitation	-	Daily Summaries (June to Sept. 2012)	Tabular Data
Relative Soil Moisture - ASCAT Metop	-	Almost Daily (June to Sept. 2012) with some data gaps	Tabular Data
GIS Data of thermal area (Sulfur Hills)	-	-	1
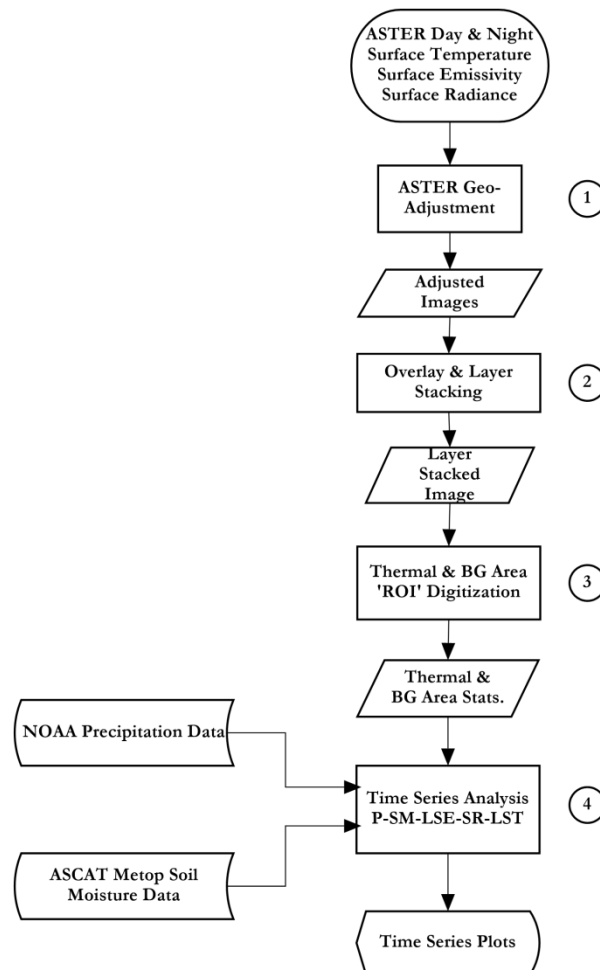
Figure 12. Remote Sensing Time Series Data Analysis Work Flow of Sulfur Hills Thermal Area in Yellowstone

Figure 12 shows the work flow of the remote sensing time series data analysis for Sulfur Hills, a thermal area in Yellowstone. The numbers included in the figure from 1 to 4 correspond to the description of the work flow which are as follows:

1. ASTER Geo-Adjustment: After collecting 4 night and 3 day time ASTER Images as summarized in Table 6 for the time period between June to September 2012, the night time ASTER Surface Kinetic Temperature, Surface Emissivity and Surface TIR Radiance images were adjusted for correctly overlaying with Day Time ASTER Images. Figure 13 provides the images of Before (A) and After (B) adjustments for night time ASTER Image of Sulfur Hills in Yellowstone. All the night time ASTER surface temperature, emissivity and surface Radiance TIR Images were corrected manually based on the polygon boundary shape file of Sulfur Hills from GIS data of Wyoming State Geological Survey (Ranz, 2015). The night time ASTER images were adjusted by editing the tie points of x and y image coordinates in the header information associated with the image file. After adjustment of ASTER Images, the boundary of the shape file of Sulfur Hills matched with the boundary of elevated surface temperature pixels in the ASTER Image.

2. Overlay & layer Stacking: After the night time ASTER images were geo-adjusted, Day and Night Surface Temperature, Emissivity and Surface Emitted Radiance Images were overlaid and layer stacked together in chronological order. Numerically, there were 12 (4 * 3 types) night time ASTER Images and 9 (3 * 3 types) day time ASTER Images which were layer stacked together. All together there were 21 ASTER night and day images of the Sulfur hills and surrounding region.

3. Thermal & Background Area Digitization: With the 21 layer stacked images the Region of Interest 'ROI' tool in ENVI was used to digitize the background area beside Sulfur Hills that had a 'homogenous' composition. The homogeneity was decided based on literature, maps, visual inspection and comparison with Google Earth Images. Similarly the anomalous area was also digitized based on the polygon boundary shape file of thermal area from GIS data. The statistics such as mean surface temperature, mean emissivity, mean emitted radiance of the anomalous area as well as background area were collected using the ROI tool for all the 21 day and night ASTER Images. The Background Area digitization is defined as in Figure 14. Both ASTER (A) as well as the corresponding Google Earth Pro (B) images are added for comparison.

4. Time Series Analysis: To know the precipitation and relative surface soil moisture states of the Sulfur hills thermal area and the background area for the desired time period (June to September 2012), NOAA and ASCAT Metop data for the same area were obtained. The rainfall data are daily summaries collected from NOAA ground monitoring station near Yellowstone lake which is the closest rainfall station to the Sulfur hills thermal area. The values of precipitation collected from the rainfall station are assumed to be the same for the Sulfur Hills and the background area because the station and thermal areas are within a distance of a few kilometres. The relative surface soil moisture information is taken directly from METOP Advanced Scatterometer (ASCAT) Soil Moisture Data Viewer maintained by Department of Geodesy and Geo-information, TU Wien (Wien, 2015). The relative surface soil moisture data values range in degrees of saturation (%) with 0 meaning completely dry and 100% completely saturated. This information is applicable for 2 cm of the top surface (Wien, 2015). Time Series information was collected from 23rd June to 18th Sept. 2012 for the gridded point data which lay closest to the thermal area of interest. It is to be noted that the pixel size (25 km with grid spacing of 12.5 km) of the relative surface soil moisture data from ASCAT covers both the background as well as the Sulfur Hills thermal area easily because the thermal area and background region size put together is relatively much smaller than a single pixel size of ASCAT Metop Satellite. The data from all the sources namely, Precipitation (P), Relative Surface Soil

Moisture (SM), Land Surface Emissivity (LSE), Surface Emitted Radiance (SR) and Land Surface Temperature (LST) were collected and various time series plots were created.

The aim of creating such a time series of P-SM-LSE-SR-LST for the Sulfur Hills thermal area in Yellowstone is to address the third research objective of examining the effects of soil moisture in detecting geothermal surface temperature anomalies with remote sensing datasets. Specifically, the aim is to investigate whether there is any relationship of soil moisture with three parameters namely, Surface Temperature, Surface Emissivity and Surface Radiance TIR of ASTER Images. In particular, to analyse whether high surface soil moisture states coincides with low surface temperature anomalies or high surface temperature anomalies or they have no effect whatsoever. The time series analysis also tests the hypothesis that soil moisture states lead to cooler thermal anomalies.

A.   Before Adjustment   B. After Adjustment
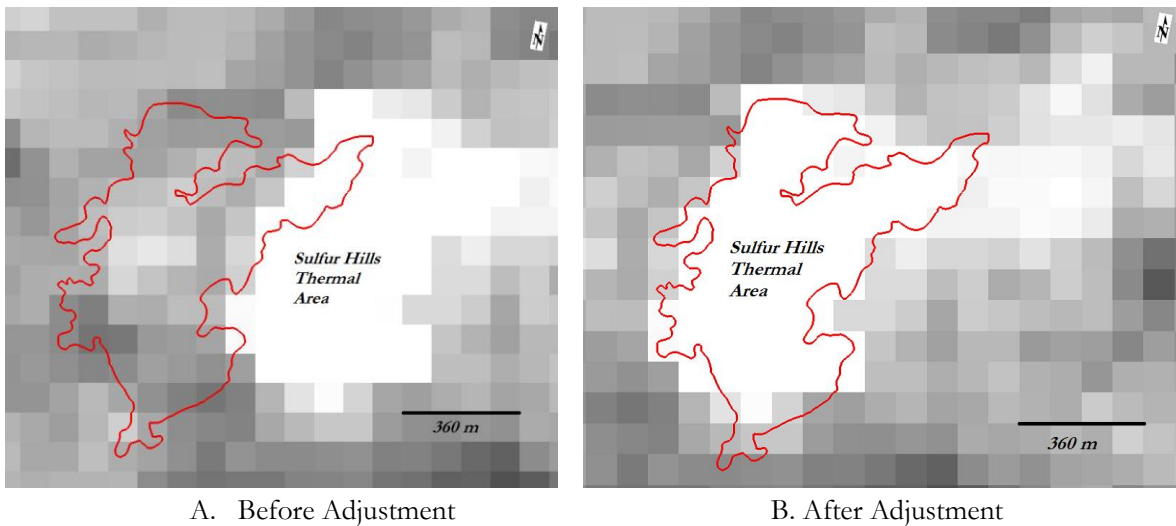
Figure 13. ASTER Night Image Geo-adjustment. A and B show the before and after geo-adjustment status of a surface temperature image. The dark areas on the image show cooler temperatures and the white areas indicate hotter temperatures. The red polygon shows the shape file of Sulfur hills thermal area overlaid on the ASTER Image.

A.   B.
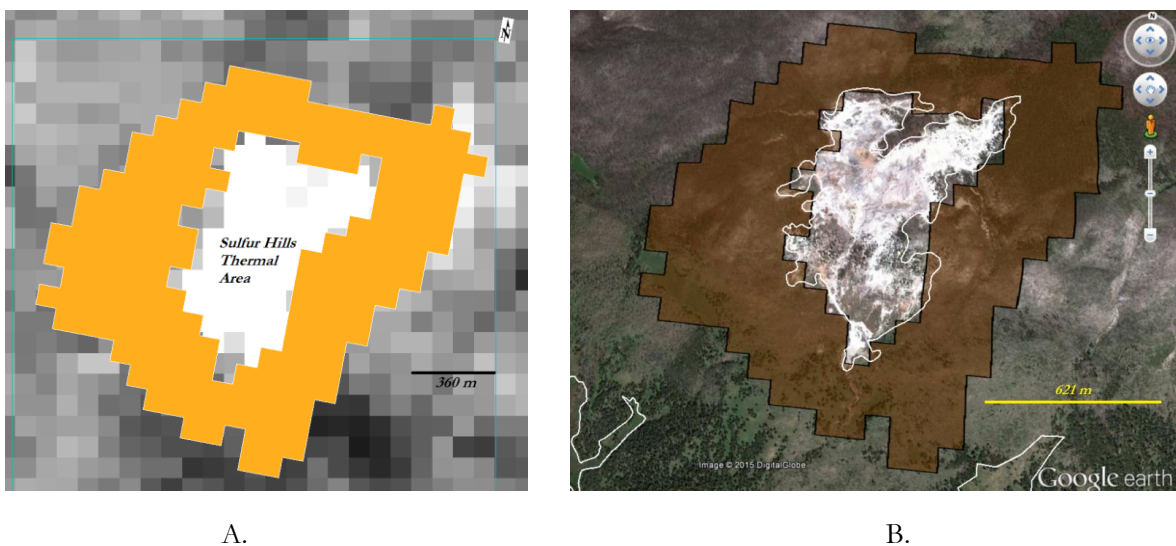
Figure 14. Background Area Digitization in ASTER Image and overlaid on Google Earth Image for comparison. A . ASTER Background Area Digitization using 'ROI'. B. Same Background Area Shape File overlaid on Google Earth Pro image.

5.2. Results

The Results are divided into four sub sections namely, (5.2.1) Overview of Time Series, (5.2.2) Time Series link to land surface temperature anomalies, (5.2.3) Time Series link to Emitted Radiance TIR and (5.2.4) Time Series link to Emissivity. The Results section ends with a short summary (5.2.5).

5.2.1. Overview of Remote Sensing Time Series Data

The results of the chronological order of ASTER Images, corresponding Precipitation summary of the day, Relative Soil Moisture amount (%) and acquisition time are summarized in Table 7. The Day time ASTER scenes are acquired after noon around 12:30 hrs and the Night time images are usually acquired around 23:30 hrs over Yellowstone. The precipitation and soil moisture columns in Table 7 are colour coded with blue shades. In addition to that, the last column of Table 7 summarizes the surface temperature anomalies which are the difference between the mean surface temperature of thermal areas and the background areas.

Table 7. Chronological order of Precipitation, Soil Moisture amount (%), Soil Moisture acquisition time, ASTER acquisition time and date. The summary of the precipitation is in millimetre per day. The last column of ASTER Δ°C is the difference in mean anomalous thermal area surface temperature and background surrounding surface temperature.

Date	Precipitation (mm/d)	SMC (%)	SMC Time	ASTER Time	ASTER Δ °C
6/12/12	0.00	40.14	5:00		
6/13/12	0.00	45.13	4:39		
6/14/12	0.00				
6/15/12	0.00	35.38	3:57		
6/16/12	0.00	34.32	3:37		
6/17/12	0.00	43.3	4:56		
6/18/12	0.00	37.45	16:51		
6/19/12	0.00	38.28	18:10		
6/20/12	0.00	25.82	17:49		
6/21/12	0.00	29.49	3:33		
6/22/12	0.00	34.85	4:53		
6/23/12	0.00	42.91	16:47	Night 23:25	10.59
6/24/12	0.00	51.55	18:06		
6/25/12	0.00	27.47	3:50		
6/26/12	0.00				
6/27/12	0.00	21.41	17:04		
6/28/12	0.00	44.29	16:44		
6/29/12	0.00	45.91	18:03		
6/30/12	0.00	22.08	3:47	Day 12:24	5.00
7/1/12	0.00				
7/2/12	0.00	26.99	4:46		
7/3/12	0.00				
7/4/12	0.00	36.22	17.59		
7/5/12	0.64	21.37	3:43		
7/6/12	0.64				
7/7/12	0.51	31.69	16:57		
7/8/12	1.78				
7/9/12	0.00	42.27	17:56		
7/10/12	0.00	32.7	3:40		
7/11/12	3.81	36.35	4:59	Night 23:13	9.19
7/12/12	1.27	85.79	4:39		

7/13/12	2.54			
7/14/12	5.08	100	3:57	
7/15/12	10.16	94.46	3:36	
7/16/12	1.27	49.57	4:56	
7/17/12	1.27	58.62	16:50	
7/18/12	0.00	50.92	18:10	
7/19/12	0.00	33	3:54	
7/20/12	0.00	28.73	3:33	
7/21/12	0.00	27.41	4:52	
7/22/12	0.00	34.1	16:47	
7/23/12	0.00	38.54	18:06	
7/24/12	0.00	12.48	3:50	
7/25/12	0.00			
7/26/12	0.00	24.16	4:49	
7/27/12	0.00	34.81	16:44	Night 23:13	10.96
7/28/12	0.00	53.61	18:03	
7/29/12	0.00	23.92	3:47	
7/30/12	0.00			
7/31/12	0.00	19.87	4:46	
8/1/12	0.00			
8/2/12	0.00	20.84	18:00	
8/3/12	0.00	13.77	3:43	
8/4/12	0.00			
8/5/12	0.00	5.67	4:42	
8/6/12	0.51			
8/7/12	0.64	38.87	17:56	
8/8/12	0.00	14.34	3:40	
8/9/12	0.00	29.9	4:59	
8/10/12	0.00	18.83	4:39	
8/11/12	0.00			
8/12/12	1.27	12.73	3:57	
8/13/12	0.00	10.79	3:37	
8/14/12	0.00	16.33	4:56	
8/15/12	0.00	9.04	16:51	
8/16/12	0.00	20.38	18:10	
8/17/12	0.00	0	3:54	Day 12:24	6.92
8/18/12	0.00	18.44	3:33	
8/19/12	0.00	10.24	4:53	
8/20/12	0.00	18.84	16:47	
8/21/12	0.00	33.4	18:06	
8/22/12	0.00	11.55	3:50	
8/23/12	0.00			
8/24/12	0.00	12.74	17:04	
8/25/12	0.00	15	16:44	
8/26/12	0.00	25.37	18:03	
8/27/12	0.00	15.36	3:47	
8/28/12	0.00			Night 23:13	12.85
8/29/12	0.00	17.44	4:46	
8/30/12	0.00			
8/31/12	0.00	12.53	18:00	
9/1/12	14.61	17.82	3:44	
9/2/12	10.03			
9/3/12	0.00	47.88	4:42	
9/4/12	0.00			
9/5/12	0.00	23.63	17:56	
9/6/12	0.00	7.44	3:40	
9/7/12	0.00	11.75	5:00	
9/8/12	0.00	0	4:39	
9/9/12	0.00			
9/10/12	0.00	0.29	3:57	
9/11/12	0.00	15.73	3:37	
9/12/12	0.00	8.55	4:56	
9/13/12	0.00	6.99	16:51	
9/14/12	0.00	22.74	18:10	

9/15/12	0.00	0	3:54		
9/16/12	0.00	26.83	3:33		
9/17/12	1.27	52.39	4:53		
9/18/12	0.00	15.48	16:47	Day 12:24	7.70
9/19/12	0.00	24.91	18:06		
9/20/12	0.00	0	3:50		
9/21/12	0.00	16.56	4:49		
9/22/12	0.00	0	17:04		
9/23/12	0.00	20.45	16:44		
9/24/12	1.27	21.34	18:03		
9/25/12	0.00	91.62	3:47		
9/26/12	0.00				
9/27/12	0.00	61.73	17:01		
9/28/12	1.27				
9/29/12	1.27	35.39	18:00		

From Table 7 it can be noted that there are some data gaps present with the relative soil moisture column of values. This is normal as ASCAT Metop satellite has a temporal frequency of 1-2 days. Another important factor which has to be taken into consideration is the size (25 km) of each pixel of ASCAT Metop which easily covers both the Sulfur Hills thermal area and the surrounding background area. Therefore, the soil moisture information provided in Table 7 is applicable to the complete area and not as separate for anomalous and background region of Sulfur hills which is being studied for soil moisture effects. It can be also seen that even though there is no precipitation (0 mm/d) for a day, still the soil moisture amount shows some values. These soil moisture values can be expected due to the fluctuations in ASCAT noises with each acquisition.

Using the surface temperature anomaly values and soil moisture information associated with each date for Sulfur Hills and background area from Table 7 the next section (5.2.2) provides details of the analysis. Emitted Radiance anomalies (5.2.3) and Emissivity differences (5.2.4) follow in the subsequent sections.

5.2.2. Time Series link to Land Surface Temperature Anomalies

The aim with this section is to describe the results of the ASTER land surface temperature anomalies and their relationship with the relative soil moisture information. This section addresses the third research objective of the effect of soil moisture in detecting geothermal surface temperature anomalies. Land surface temperature anomaly is the mean surface temperature difference between the anomalous pixels and the surrounding background pixels of Sulfur Hills. Figure 15 shows graphically the difference in mean land surface temperature values between the anomalous pixels and the background pixels from Sulfur Hills. The black circular dots correspond to the night time surface temperature anomalies and the red squares correspond to the day time surface temperature anomalies. The anomaly values are in degree Celsius. Soil moisture information is shown with the blue coloured columns ranging from 0 to 100% degree of saturation with the scale provided on the left vertical axis. Data gaps in soil moisture can also be noticed clearly. The right vertical axis shows the scale of the temperature anomaly values. Focus is made on 28th August 2012 night time surface temperature anomaly of 12.85°C with a red dashed outline circle in addition to 27th July 2012 night time surface temperature anomaly of 10.96°C also highlighted with a red dashed circle. 12.85°C and 10.96°C are the highest temperature anomaly difference out of all the 7 night time and day time images. In general it can be noticed that night time (black circular dots) temperature anomaly values are greater than day time anomalies relatively.
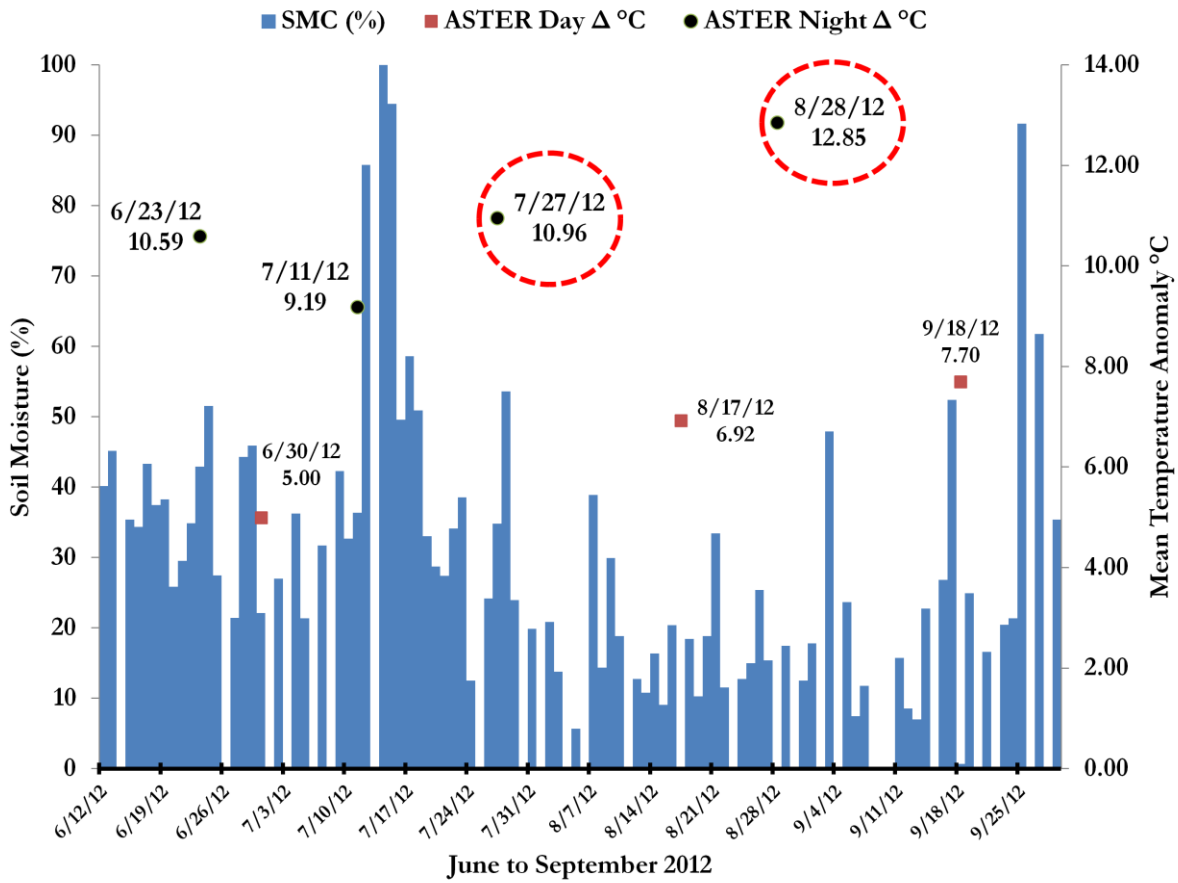
Figure 15 Graphical Representation of Soil Moisture (%) and Mean Surface Temperature Anomalies associated with ASTER Land Surface Temperature data. The horizontal axis shows the dates from June to September 2012. The blue coloured vertical bars indicate the soil moisture (%) in degree of saturation from 0 to 100% scale on the left vertical axis. The secondary vertical axis on the right shows the scale of the mean surface temperature in degree Celsius. The black circular dots are the 4 night time mean surface temperature differences between the anomalous pixels and the background pixels of Sulfur Hills. The 3 red coloured squares are the day time mean surface temperature difference. The two highest night time temperature anomaly of 12.85°C and 10.96°C is highlighted with a red dashed circle.

Once the surface temperature anomalies corresponding to each date are known it is crucial to examine closely the soil moisture conditions of each surface temperature anomaly. Therefore, Table 8 summarizes the results of all the 7 individual ASTER temperature anomaly dates and soil moisture information for the same associated dates. The colour codes of blue shades are added for clarity for the soil moisture column in Table 8. Similarly, ASTER temperature anomaly Δ°C column also is colour coded for clarity showing the red colour with the lowest temperature anomalies and the light green colour with the highest temperature anomalies. From the table it can be noticed that day and night are separated in first three and last four rows respectively. It is because day and night time temperature anomaly values cannot be interpreted in the same way. Night time soil moisture data values are all higher than the day time soil moisture values. For night time the highest temperature anomaly of 12.85 °C is found on 28th August 2012 as mentioned earlier. However, there is a data gap present exactly on the same day. The second highest temperature anomaly of 10.96°C on 27th July 2012 night time has the least soil moisture value of 34.81% after comparing 3 night time images' soil moisture value. Highest night time soil moisture condition on 23rd June shows a value of 42.91% and corresponds to a temperature anomaly of 10.59°C. For the day time, it can be noted that the highest soil moisture information of 22.08 % corresponds to the lowest temperature anomaly of 5.00°C out of the three dates.

Table 8 Summary of surface temperature anomaly and soil moisture information corresponding to each ASTER image of Sulfur Hills. The soil moisture value column SMC (%) are colour coded in blue shades with the light blue corresponding to the lowest value and the dark blue shade corresponding to the highest value. The ASTER Δ °C column is also colour coded with red (lowest value) to light green (highest value). The first three rows correspond to day time and the last 4 rows correspond to night time. 28th Aug. soil moisture information has a data gap.

Date	SMC (%)	ASTER Δ °C	
6/30/12	22.08	5.00	DAY
8/17/12	0	6.92	
9/18/12	15.48	7.70	
6/23/12	42.91	10.59	NIGHT
7/11/12	36.35	9.19	
7/27/12	34.81	10.96	
8/28/12		12.85	
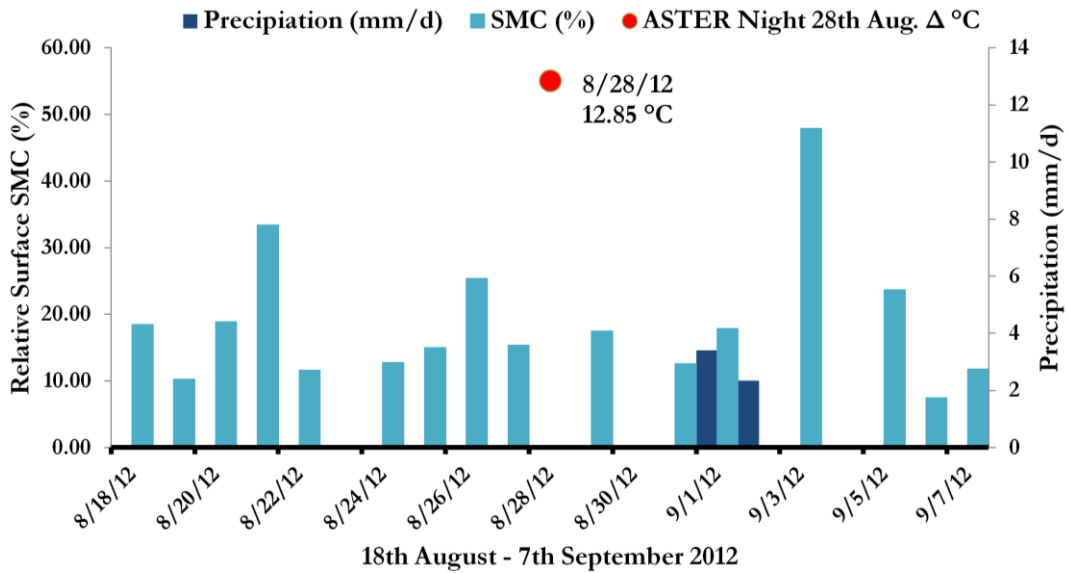
Figure 16 Antecedent precipitation before 28th August for data gap interpolation. Light blue columns on the graph are the soil moisture values corresponding to each date. The left vertical axis scale corresponds to relative soil moisture information. The dark blue column is the precipitation value with the right vertical axis showing the scale of precipitation in mm/d. The red circular dot corresponds to the temperature anomaly of 12.85°C for 28th August.

The highest surface temperature anomalies of 28th August correspond with a soil moisture data gap. But it is possible to interpolate the missing value by analyzing the antecedent precipitation information. Included in Figure 16 is a graph which shows the pattern of precipitation (dark blue column) and soil moisture (light blue column). The red circular dot stands above the 28th August date line. Since the time period

before 28th August was a long and dry period as can be seen from 0 mm/d precipitation, it can be assumed that the soil moisture value on 28th August falls somewhere between 15.36 % (27th August) and 17.44 % (29th August). Therefore an average value is taken at 16.4 % relative soil moisture for 28th August night time. This value of 16.4 % relative soil moisture can be filled in the data gap cell of Table 8 corresponding to 28th August surface temperature anomaly of 12.85°C. After fitting the interpolated soil moisture information of 28th August it can be inferred that the lowest soil moisture out of the four night time temperature anomalies are found to be associated with the same interpolated 16.4% relative soil moisture value followed by the second highest temperature anomaly of 10.96°C on 27th July corresponding to the second lowest relative soil moisture of 34.81 %.

With the surface temperature anomalies and soil moisture relationship established, it is equally important to understand how the soil moisture information corresponds to the Surface emitted radiance anomalies in the ASTER TIR. Therefore the next section (5.2.3) describes the emitted radiance anomalies and their relationship with soil moisture from the same time series data analysis. It is to be noted here that one of questions raised in the research problem in section 1.3 was to understand how soil moisture affects emitted radiance in the ASTER TIR (8 to 12 μm).

5.2.3.   Time Series link to Land Surface Emitted Radiance Anomalies

The aim with this section is to present and explain the results of the ASTER land surface emitted radiance and their differences between the anomalous pixels and the background pixels and how they correlate with the soil moisture information for the Sulfur Hills thermal area.

Figure 17 shows the time series data points of relative soil moisture and mean Surface Emitted Radiance in ASTER TIR of thermal areas (coloured circles) and the background areas (coloured squares). Clearly, the day time (30th June, 17th August and 18th September) Surface Emitted Radiances from both the thermal area as well as the background area is higher compared to the night time. From the four night time scenes, the focus is on one 28th August night time scene highlighted with a rectangular black dashed box. The Surface emitted radiance on 28th August night seems to be the highest out of all the four night time scenes. The striking feature from the graph of 28th August is the clear separation between the coloured circles (Surface Emitted Radiance of thermal area or anomalous area) and the coloured squares (Surface Emitted Radiance of background area). Although there is a separation corresponding to 23rd June scene also, this separation is smaller than 28th August. All other night and day scenes show overlap between the mean surface emitted radiance of background and anomalous pixels in ASTER TIR. In order to see the differences between the anomalous surface emitted radiance and the background surface emitted radiance in all ASTER TIR bands another graph has been created. Figure 18 is a combination of a table as well as a graph. The figure shows the mean surface emitted radiance differences for all day and night scenes in ASTER TIR. The mean surface emitted radiance differences are found by subtracting the mean surface emitted radiance value of background pixels by the mean surface emitted radiance of anomalous pixels in the same ASTER TIR Band for all the day and night scenes. Since the surface emitted radiance values of thermal pixels are higher than the background, all differences are positive as is shown in
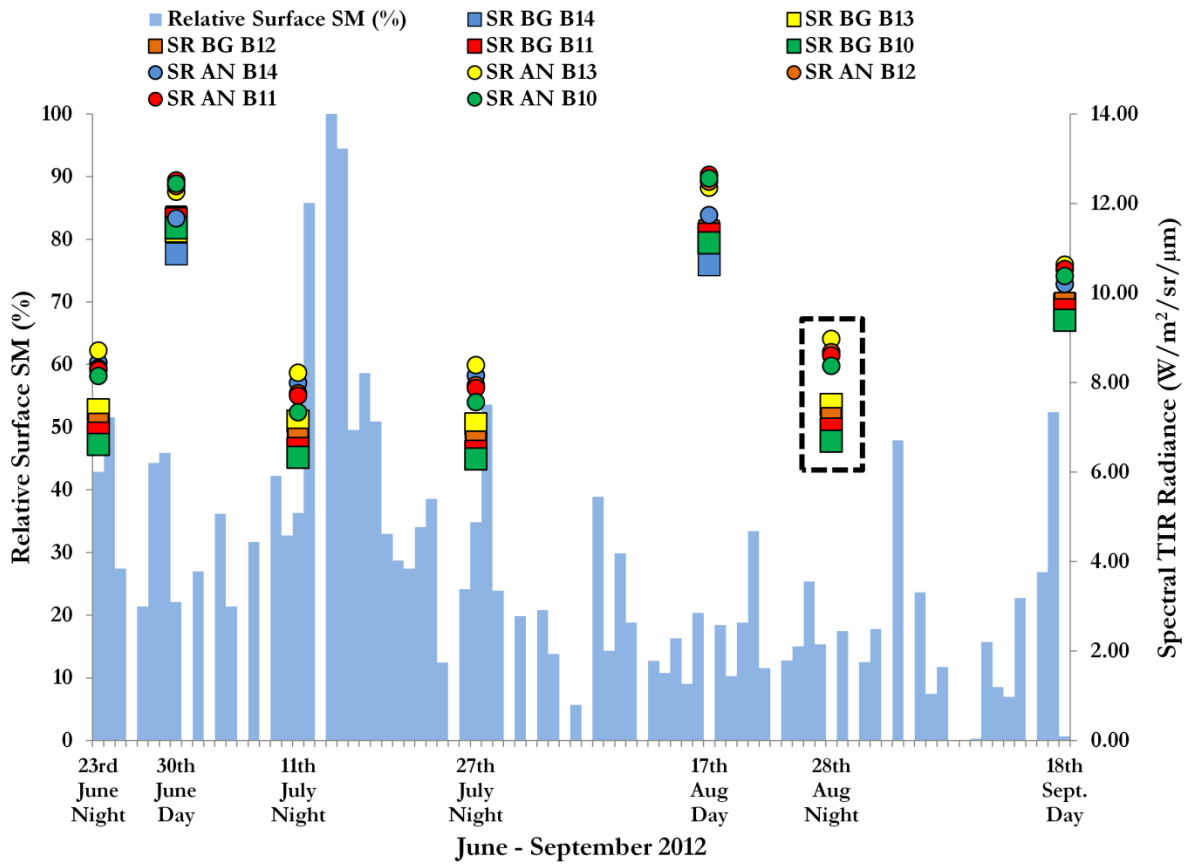
Figure 17 Time Series of SM & Emitted TIR Radiance of Mean Background and Anomalous pixels. The horizontal axis shows the different dates of ASTER Day & Night of Image acquisition. The light blue columns show the relative soil moisture with the primary vertical axis on the left from 0 to 100%. The secondary vertical axis on the right shows the Spectral Emitted TIR radiance values in units of W/m²/μm/sr. The coloured squares represent the mean background Surface Emitted TIR radiance values from Band 10(B10) to Band 14 (B14) for Sulfur Hills. Similarly the coloured circles represent mean anomalous Surface Emitted TIR radiance values from Band 10(B10) to Band14 (B14) for the thermal anomalous area of Sulfur Hills. SR stands for Surface Emitted Radiance on the graph, BG stands for Background and AN stands for Anomalous area. The black dashed rectangle highlights the emitted radiance on 28th August.

the table of Figure 18. The figure shows the differences as coloured lines with coloured circular data points. Each circular coloured data point corresponds to the values in the table. The relative soil moisture information is also included in the graph with the blue column showing the value of each soil moisture state for the corresponding day and night scene. The right vertical axis shows the scale of relative soil moisture and the left vertical axis shows the units of difference in surface emitted radiance in W/m²/μm/sr. The black rectangular box is used to highlight the largest differences found in all the ASTER TIR bands for 28th August Night time scene. It is to be noted here that the relative soil moisture value for 28th August used in Figure 18 is 16.4% which was interpolated in the previous section. Out of all the day and night scenes, 28th August shows the highest differences in mean surface emitted radiance between the anomalous pixels of Sulfur Hills and background pixels in all the 5 ASTER TIR Bands. For Day Time Images, the differences are highest on 17th August from Figure 18. While Comparing Day and Night it is interesting to note that the highest Radiance difference for the Night time is higher than the highest Radiance difference for the day time.

Emitted Radiance Anomaly Difference - ASTER TIR

	23rd June Night	30th June Day	11th July Night	27th July Night	17th Aug Day	28th Aug Night	18th Sept Day
SMC (%)	42.91	22.08	36.35	34.81	0	16.4	15.48
B10 (8.2 μm)	1.53	0.98	1.01	1.27	1.44	1.68	0.99
B11 (8.6 μm)	1.41	0.85	1.17	1.41	1.32	1.65	0.91
B12 (9 μm)	1.23	0.68	1.00	1.26	1.10	1.47	0.75
B13 (10.6 μm)	1.33	0.88	1.08	1.32	1.23	1.47	0.89
B14 (11.3 μm)	1.18	0.79	0.96	1.17	1.11	1.32	0.81
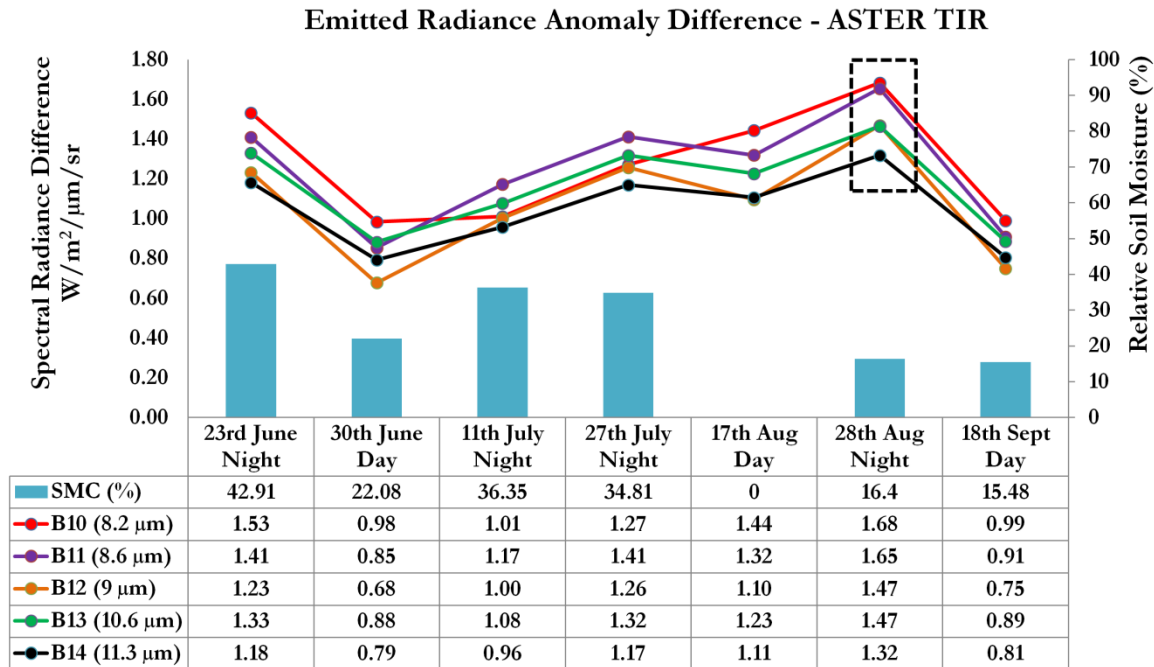
Figure 18 Surface Emitted Radiance Difference for Day and Night Time in 5 ASTER TIR Bands for Sulfur Hills. The figure also contains an associated table for each date containing the relative soil moisture information and the difference in mean surface emitted radiance values between the anomalous pixels (thermal areas) and background pixels (background area) in each ASTER TIR Band (B10 to B14) shown with a coloured line with same coloured circles as data points. The blue column on the graph corresponds to the relative soil moisture value in % for each date. The right vertical axis shows the relative soil moisture scale. The left vertical axis is the mean surface emitted radiance difference values in W/m²/μm/sr. The black dashed rectangular box highlights the surface emitted radiance difference for 28th August.

The highest parameter values of surface emitted radiance anomalies and surface temperature anomalies correspond to the lowest relative soil moisture state of 28th August night time scene out of all the four night time scene. To complete the picture, it is essential to scrutinize the emissivity conditions over the same set of ASTER Images. Therefore, the next section (5.2.4) deals with the results of land surface emissivity and soil moisture relation.

5.2.4. Time Series link to Land Surface Emissivity

The aim with this section is to present the results of the ASTER land surface emissivity and the differences between the emissivity of anomalous pixels and the background pixels and correlate them with the soil moisture information for the Sulfur Hills thermal area and background area surrounding the thermal region.
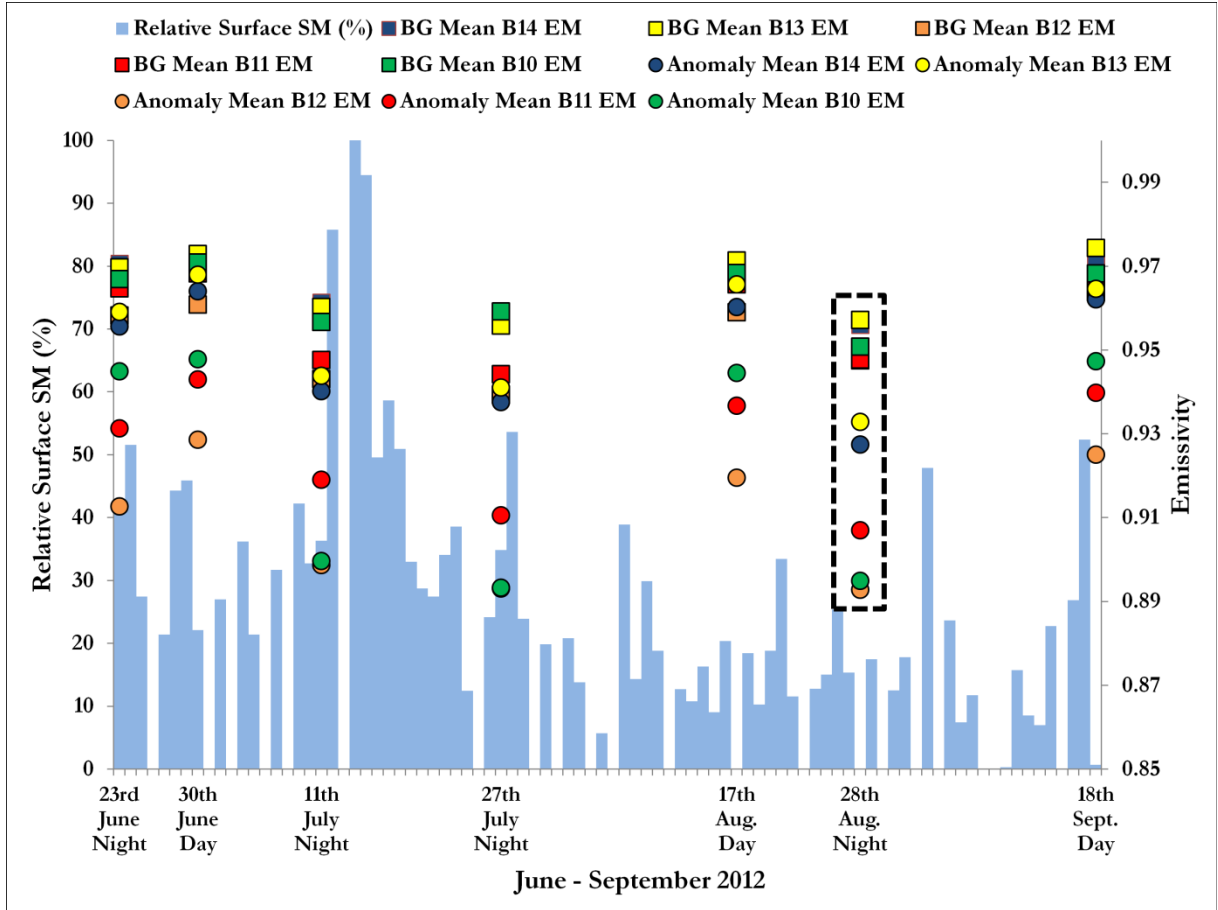
Figure 19 Time series graph of relative soil moisture, mean background and mean anomalous emissivity in ASTER Bands for 7 day and night scenes. The horizontal axis shows the different dates of ASTER Day & Night Image acquisition. The light blue columns show the relative soil moisture with the axis on the primary vertical axis on the left from 0 to 100%. The secondary vertical axis on the right shows emissivity. The coloured squares represent the mean background emissivity values from Band 10(B10) to Band 14 (B14) for Sulfur Hills. Similarly the coloured circles represent mean anomalous emissivity values from Band 10 (B10) to Band14 (B14) for Sulfur Hills. The black dashed rectangular box highlights the emissivity on 28th August Night. BG stands for background pixels and anomaly stands for anomalous pixels. EM stands for emissivity.

Figure 19 shows the time series of mean emissivity, both for the background as well as for the anomalous pixels of Sulfur Hills in the 5 ASTER TIR bands. The horizontal axis shows the day and night time ASTER Image acquisition dates, vertical axis on the left is Relative Surface SM (%) and vertical axis on the right is Emissivity. The coloured circles correspond to Mean Anomalous pixels emissivity at ASTER wavelengths and the coloured squares correspond to Mean Background pixels' emissivity. Overall the emissivity values found in day and night time in remotely sensing ASTER TIR are high (0.89-0.97). The clear difference which can be noticed from Figure 19 is day time emissivities are higher relative to night time emissivity. It can be also noted from the graph that the mean emissivity values of anomalous pixels are relatively lower than the mean emissivity values of the background pixels in ASTER. In some cases (where the coloured squares and coloured circles overlap) the background and anomalous emissivity values are closer. The highlighted black dashed rectangle over 28th August night time scene is to show that the emissivity patterns are different to other day and night scenes. The difference is the clear separation of anomalous and background emissivity even though the differences are quite small. No mean emissivity values of the anomalous pixels overlap with the mean emissivity values of background pixels for 28th August night time scene.

Emissivity Difference - ASTER TIR

	23rd June Night	30th June Day	11th July Night	27th July Night	17th Aug Day	28th Aug Night	18th Sept Day
SMC (%)	42.91	22.08	36.35	34.81	0	16.4	15.48
B10 (8.2 μm)	0.02	0.02	0.06	0.07	0.02	0.06	0.02
B11 (8.6 μm)	0.03	0.03	0.03	0.03	0.03	0.04	0.03
B12 (9 μm)	0.05	0.03	0.04	0.05	0.04	0.05	0.04
B13 (10.6 μm)	0.01	0.00	0.02	0.01	0.01	0.02	0.01
B14 (11.3 μm)	0.01	0.01	0.02	0.02	0.01	0.03	0.01
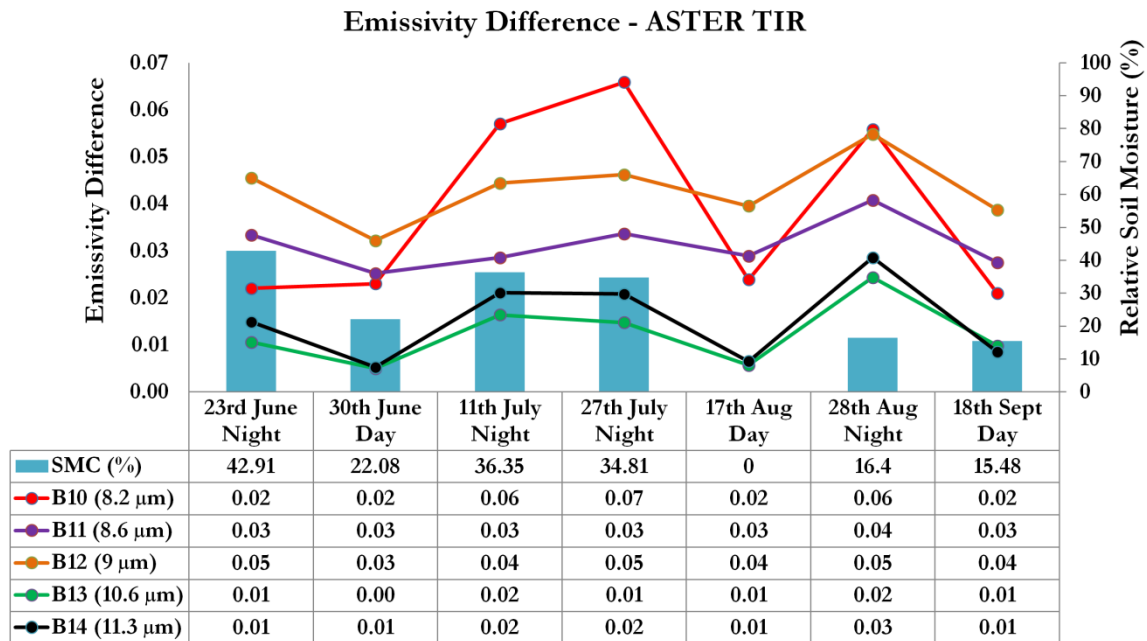
Figure 20 Emissivity Difference for Day and Night Time in 5 ASTER TIR Bands for Sulfur Hills. The figure also contains an associated table for each date with the relative soil moisture information and the difference in mean emissivity values between the anomalous pixels (thermal areas) and background pixels (background area) in each ASTER TIR Band (B10 to B14) shown with coloured line with same coloured circles as data points. The blue column on the graph corresponds to the relative soil moisture value in % for each date. The right vertical axis shows the relative soil moisture scale. The left vertical axis is the mean emissivity difference.

Figure 20 shows the difference in mean emissivity values for night and day ASTER TIR Bands for background and anomalous area of Sulfur Hills. There is also an associated table with the graph which is arranged date wise in each column and each row represents 5 ASTER TIR bands and a row containing the relative soil moisture values. The relative soil moisture values are also represented by a blue column. The right vertical axis is the unit for the relative soil moisture in %. The left vertical axis shows the emissivity difference. Although, in Figure 19 there was a clear separation of anomalous and background emissivity, the differences of emissivity in Figure 20 do not show any clear pattern for 28th August night time scene, although highest emissivity differences are found in Band 14 and Band 11.

5.2.5.   Summary of Time Series Results

Time series data analysis of three parameters namely, surface temperature anomalies, surface emitted radiance anomalies and surface emissivity, provided with the following results:

Highest surface temperature anomalies were found to be associated with lowest soil moisture conditions in night time. Lowest surface temperature anomalies were found in day time when the highest soil moisture conditions were present. Surface emitted radiance results showed that highest differences are found when the soil moisture conditions are low in night time images. The emissivity results showed that the mean emissivity values of background area is relatively higher than the mean emissivity value of thermal area. Moreover, the lowest soil moisture conditions in night time ASTER TIR showed that the emissivity values do not overlap with the background and thermal area.

6.   DISCUSSION

The discussion section is divided into six sub-sections which discusses the (6.1) thermal infrared measurements of dry and wet soil, (6.2) synthetic data model, (6.3) remote sensing time series data analysis, (6.4) Integration of synthetic data model and remote sensing results, (6.5) limitations and uncertainties applied in remote sensing analysis (6.6) geothermal surface anomaly definition

6.1.   Discussion on Thermal Infrared Measurements of Dry and Wet Soils

This section is on the discussion of thermal infrared measurements of dry and wet soils used in this study in Chapter 3. It is divided into three paragraphs. The first paragraph discusses the justification, the second paragraph discusses the actual results and the third paragraph ends with the uncertainties.

In this research the focus was on the effect of soil moisture on emissivity. Other parameters related to soil moisture that possibly influences geothermal anomaly detection such as albedo, land surface temperature, emissivity, thermal inertia, and latent heat flux were neglected. In the lab the relation between soil moisture and emissivity in the ASTER TIR bands were studied. An experimental setup for measuring emissivity of dry and wet soil was beneficial for addressing the research problem of the effect of soil moisture on emitted radiance. Therefore, it was not necessary to use the actual soil samples from the study area. Nevertheless, the soil samples, loam and especially sandy loam used in this study have similar mineralogical characteristics like the one found in Yellowstone Caldera which are dominated by minerals such as quartz and K-feldspars due to the presence of rhyolite and tuff (Parks, 2016).

The experimental results showed that with increasing soil moisture the emissivity also increases which is in agreement with previous research (Wang et al., 2015; Sanchez et al., 2011; Hulley et al., 2010; Mira et al., 2007; Salisbury & D'Aria, 1992). Loam soil emissivity plots (Figure 4) show a slight increase after further drying out from 4.43% SMC state until it reaches 0.96 at 0% SMC in the 8-9μm range. This reversal in trend may be caused due to the formation of cracks in the soil as it was drying out. Similar phenomena have been reported in literature (Sanchez et al., 2011). With sandy loam emissivity plots (Figure 3), the same kind of reverse trend of increasing emissivity values with decreasing soil moisture conditions were not observed, although tiny cracks were also present here. The reason could be attributed to the difference in mineralogical composition of sandy loam soil which is dominated by quartz and k-feldspars as compared to loam soil which is more clay rich relatively.

The uncertainties and errors in extracting emissivity values of dry and wet soils from lab measurements can be influenced by a number of circumstances. It is tricky to keep the top few micrometers of the soil surface wet homogeneously like the rest of the soil in the petridish and to take representative measurements, although the depth of the soil was limited to 2 cm of the petridish. The time difference between the spectral measurements and the gravimetric SMC % weight measurements can introduce uncertainties. Longer the time difference, greater will be the errors. Random errors in the FTIR instrument can introduce the largest errors in the result.

6.2.   Discussion on Synthetic Data Modelling

This section discusses the results of the synthetic data analysis to simulate the effects of soil moisture in detecting geothermal surface temperature anomalies. It is divided into three sub-sections namely, (6.2.1) Discussion on day and night differences, (6.2.2) Discussion on dry and wet soil combinations, (6.2.3) Discussion on sensor noise effects. The section ends with a short paragraph on uncertainties of synthetic data model.

6.2.1.   Discussion on day and night differences

This discussion is about the differences between day and night for thermal anomaly detection. In this study two different geothermal areas representing different climatic and geological settings were chosen in order to see the differences in thermal anomaly detection both for day and night conditions in Yellowstone and Olkaria. The results of the synthetic data plots from Section 4.4.3, Figure 9 (ii, iv) show the differences between Yellowstone and Olkaria for night time conditions with an overall mean detection rate of 0.85 and 0.81 respectively. Figure 9 (i, iii) synthetic data plots show the differences for day time conditions in Yellowstone and Olkaria with an overall mean detection rate of 0.54 and 0.50 respectively. The mean background surface temperature and standard deviation (Table 4) for day time in Yellowstone and Olkaria extracted from ASTER satellite temperature images are higher than night time. Therefore, the reason for worse anomaly detection rates during day time is due to the addition of solar heating effects which does not allow sufficient contrast between the background and the anomalous thermal features to be developed. At night the conditions are more suitable for thermal anomaly detection because the background area cools down gradually from dusk until dawn while the thermally emissive areas remain warm and hot depending on the source of sub surface heat energy. The findings are in line with previous studies (Coolbaugh et al., 2007; Vaughan et al., 2010). Uncertainties can be mostly because of digitization on ASTER Images for extracting mean background surface temperature and standard deviation.

6.2.2.   Discussion on dry and wet soil combinations

This discussion is about the dry and wet soil emissivity combinations used for thermal anomaly detection. The dry and wet soil emissivities are introduced in the background and anomalous pixels for thermal anomaly detection. 16 combinations of dry and wet soil were used in the background and anomalous pixels for thermal anomaly detection. The setting is for a night time condition in Yellowstone. In order to simulate the effects of soil moisture in detecting geothermal surface temperature anomalies, dry and wet soil emissivity measurements were used in the synthetic model. A new table (Table 9) is introduced to discuss the results in Table 5 from Chapter 4, Section 4.4.4. Table 9 summarizes the ranks of 16 combinations of anomaly detection scenarios borrowed from Table 5. The first column corresponds to the numbers of anomaly detection plots in Figure 11. The overall mean detection rates are arranged from the best on the top row to the worst at the bottom row. The emissivity Δ difference column is the difference in emissivity values of Band 14 in ASTER TIR associated with the anomalous pixel and the background pixel. Each row represents a combination scenario of dry and wet soil emissivity used either with the background pixels or the anomalous pixel.

Table 9 Rank table of 16 Anomaly Detection Combinations. The Sr. No. column stands for the serial number of Table 5 and Figure 11 anomaly detection plots in Chapter 4, Section 4.4.4. The Ranks column is colour coded with the best detection rates corresponding to the green colour and the worst detection rates corresponding to the red colour. The column of Emissivity Δ stands for the emissivity value difference between the anomalous pixel and the background pixel in Band 14 of ASTER TIR at 11.3μm wavelength. The rows are divided into best, intermediate and worst detection rates.

Sr.No.	Background Pixels	Anomalous Pixel	Overall Mean Detection Rate	Std. Dv.	Ranks	Emissivity Δ (11.3 μm)	
iii (A)	Dry Loam	Wet Loam	0.752	0.403	1	0.028	Best Detection Rates
v (A)	Dry Loam	Wet Sandy Loam	0.751	0.402	2	0.030	
iv (A)	Dry Sandy Loam	Wet Sandy Loam	0.748	0.404	3	0.022	
vi (A)	Dry Sandy Loam	Wet Loam	0.747	0.404	4	0.020	
vii (A)	Dry Loam	Dry Sandy Loam	0.745	0.405	5	0.008	Intermediate Detection Rates
i (A)	Wet Loam	Wet Loam	0.742	0.407	6	0	
viii (A)	Wet Loam	Wet Sandy Loam	0.742	0.406	6	0.002	
i (B)	Dry Loam	Dry Loam	0.741	0.408	7	0	
viii (B)	Wet Sandy Loam	Wet Loam	0.741	0.407	7	-0.002	
ii (A)	Wet Sandy Loam	Wet Sandy Loam	0.74	0.408	8	0	
ii (B)	Dry Sandy Loam	Dry Sandy Loam	0.74	0.408	8	0	
vii (B)	Dry Sandy Loam	Dry Loam	0.737	0.409	9	-0.008	
vi (B)	Wet Loam	Dry Sandy Loam	0.733	0.41	10	-0.020	Worst Detection Rates
iv (B)	Wet Sandy Loam	Dry Sandy Loam	0.732	0.411	11	-0.022	
iii (B)	Wet Loam	Dry Loam	0.73	0.413	12	-0.028	
v (B)	Wet Sandy Loam	Dry Loam	0.728	0.412	13	-0.030	

The rows in Table 9 are divided into three classes of best, intermediate and worst detection rates based on the criteria that the first 4 rows (Ranks 1 to 4) represent scenarios when the anomalous pixel is wet and the background is dry with the 4 highest overall mean detection rate. The last 4 rows (Ranks 10 to 13) in Table 9 are designated as worst class when the background pixels are wet and the anomalous pixel is dry with the lowest overall mean detection rates. Rest of the rows (Ranks 5 to 9) are included in the intermediate scale of detection rate. It can be also noticed that two scenarios share the same Ranks (Ranks 6, 7&8) based on the same overall mean detection rate.

Best Detection Rates: The best detection rates from Rank 1 to Rank 4 in Table 9 are achieved when the anomalous pixel is covered by wet soil and the background is covered by dry soil. The reason for these better detection rates from Ranks 1 to 4 is because, the emissivity values of wet soils are generally higher which tend towards a black body in comparison to a dry state of soil which is relatively at lower emissivity. Therefore the anomalous area with higher surface temperature and higher emissivity has an elevated emitted radiance. The higher emitted radiance produces better contrast compared to the background which is at a lower emitted radiance due to lower emissivity and lower surface temperature. The emissivity differences in the last column of Table 9 are taken from the lab measured dry and wet soils resampled to ASTER TIR Band 14 (11.3μm). The highest emissivity values for all the ASTER TIR Bands for both dry and wet soils were found in Band 14. They also showed the least variation due to soil moisture in 11-12μm as described in Chapter 3. Therefore Band 14 emissivity value differences were used for this discussion. Emissivity Δ column in Table 9 shows that the patterns of positive emissivity differences between the anomalous and the background pixels consisting of dry and wet soils have some correlation corresponding

to top (1-4) ranks of best detection rates. It was expected that the highest emissivity difference for the combination scenario of the anomalous pixel and the background pixel consisting of Wet Sandy Loam and Dry Loam respectively would have given the best detection rate because of the largest emissivity difference in Band 14 of ASTER TIR. However, it is possible that due to rounding errors associated with the synthetic model simulation in IDL, Rank 1 and Rank 2 may fluctuate.

Worst Detection Rates: The lowest detection rates (Ranks 10 to 13) in Table 9 are associated with the last 4 rows when the scenario is of the background pixels covered with wet soils and the anomalous pixel covered with dry soils. On the contrary to ranks 1 to 4 when the conditions are reversed in ranks 10 to 13 when the background is wet and the anomalous area is dry, the detection rates are worse because the spectrally emitted radiance contrast between the background and anomalous area is reduced. This is due to the fact that the background pixels attains higher emissivity when they are covered with wet soil than the anomalous pixel which are at lower emissivity covered with dry soils even though the anomalous pixel is at a higher surface temperature. The worst ranks of anomaly detection rates from 10 to 13 are also supported by negative emissivity differences between the background pixels and the anomalous pixel.

Intermediate Detection Rates: will be discussed in Section 6.4 while elaborating on integration of synthetic model and remote sensing results.

The best (Ranks 1 to 4) and worst (Ranks 10 to 13) detection rates from Table 9 are in line with the expected Planck's function calculation because the emitted radiance is dependent on temperature, emissivity and wavelength. Therefore if the anomalous pixel which anyway has a higher temperature gets high emissivity due to increased moisture content the emitted radiance will increase according Planck's function in a given wavelength. On the other hand, the relatively low temperature and low emissivity background will achieve a lower emitted radiance in the same wavelength band. Similarly, when Planck's function is applied to a wet background (high emissivity) with low temperature and dry (low emissivity) anomalous area (high temperature) the emitted radiance contrast between the anomalous area and background area is reduced. However, the synthetic model did not take into consideration the changes in land surface temperature when there are changes in soil moisture. This research only focused on changes in emissivity with variation in soil moisture. Coolbaugh et al.(2007) stated that cooling effects are observed in areas where there is higher moisture content because of loss of heat through latent heat fluxes. However, this study cannot be compared one-to-one with the study of Coolbaugh et al.(2007) because the latent heat fluxes were not considered in this research.

6.2.3. Discussion on sensor noise effects on thermal anomaly detection

This section shortly summarizes the discussion on the effects of sensor noise on thermal anomaly detection. From the results of anomaly detection plots as shown in Figure 11 (A – without sensor noise, B- with sensor noise), the overall difference in mean detection rate is 0.008 with the sensor noise added for a night time scenario in Yellowstone. This is due to the addition of the Noise Equivalent difference in Temperature (NEdT) value of 0.3°K (Gillespie et al., 1998) to the thermal anomaly criteria. The thermal anomaly detection criterion is based on a temperature higher than $\mu + 2\sigma$ of the background. Therefore, when the NEdT value is added to the criterion, the thermal anomaly detection threshold increases leading to overall lower detection rates. The uncertainties in thermal anomaly detection can arise when the NEdT value increases due to sensor deterioration.

6.3. Discussion on Remote Sensing Time Series Data Analysis

This section is about the discussion of remote sensing data analysis results that were based on three parameters namely land surface temperature, surface emitted radiance and emissivity for examining soil moisture effects in detecting geothermal anomalies. The discussion is divided into four sections expounding on the three parameters and concluding with the uncertainties and limitations to the methods applied in real data analysis.

6.3.1. Discussion on Land Surface Temperature Anomalies

The difference between the mean surface temperature of anomalous pixels (geothermal area) and the mean surface temperature of background pixels (non geothermal area) in Yellowstone from a particular date were used for correlating with relative surface soil moisture information from the same date. The results in Figure 15, Table 8 and Figure 16 in Chapter 5, Section 5.2.2 show that the highest surface temperature anomalies of 12.85°C and 10.96°C are found in night time conditions when the least relative soil moisture of 16.4% and 34.81% are present out of 4 night time ASTER Images. The 16.4% relative soil moisture information is based on an interpolation. The same soil moisture information is applicable for both the background as well as the anomalous pixels because of the coarse resolution of ASCAT Metop covering both the area with a single pixel value. The reason for highest temperature anomalies to be associated with low soil moisture conditions is because with less soil moisture over the background and anomalous pixels the temperature contrast between the anomalous and background are better developed. But when the background and anomalous area is saturated with moisture both the areas have higher emitted radiance but the contrast is reduced leading to lower thermal anomaly detection. However when comparing with the study of Coolbaugh et al.(2007), it can understood that cooler anomalies are produced due to evaporative cooling when there is higher moisture content and when the moisture content is low the evaporative cooling is less leading to higher surface temperature anomalies.

The uncertainties are mainly due to the differences in time of ASTER surface temperature and ASCAT Metop relative soil moisture information and background area digitization.

6.3.2. Discussion on Surface Emitted Radiance Anomalies

The difference between the mean emitted radiance of anomalous pixels (geothermal area) and the mean emitted radiance of background pixels (non geothermal area) in Yellowstone in ASTER TIR from a particular date, were used for correlating with relative surface soil moisture information from the same date. The results in Figure 17 and Figure 18 in Chapter 5, Section 5.2.3 show that the highest surface emitted radiance anomalies are found to be associated with the night time conditions when there was least relative soil moisture (28th August, 2012 – 16.4%). The highest emitted radiance anomalies were found in all the ASTER TIR Bands for the same date. During least soil moisture states, the emitted radiance contrast between the anomalous pixels and the background pixels are developed clearly as compared to a state when the soil moisture is equally high for both anomalous and background area. The high soil moisture conditions can cause to have lesser emitted radiance contrast as well as cooling effects due to loss of heat because of evaporative cooling. The emitted radiance in TIR is a function of the emissivity and land surface temperature. Therefore, if there are large errors in emissivity and land surface temperature, it will directly affect the surface emitted radiance in ASTER TIR. Emitted radiance from Land surfaces are estimated by performing atmospheric corrections on raw ASTER TIR data. The products ordered from LPDAAC were already atmospherically corrected therefore it was not corrected for any other atmospheric

6.3.3. Discussion on Land Surface Emissivity

The mean emissivity of anomalous pixels (geothermal area) and the mean emissivity of background pixels (non geothermal area) in Yellowstone from a particular date in ASTER TIR, were used for correlating with relative surface soil moisture information from the same date. The results in Figure 19 in Chapter 5, Section 5.2.4 show that the mean emissivities of background pixels are relatively higher than the mean emissivity of anomalous pixels in all ASTER TIR Bands. This could be due the type of surface material the thermal area and the background area is composed of. Due to the presence of quartz rich minerals in the thermal area the emissivity of the anomalous pixels are low. The background pixels composed of bare soil and a mix of vegetation which may be the reason for the higher emissivity as compared to anomalous pixels from Sulfur Hills thermal area. The highest variation in emissivity difference as shown in Figure 20, is associated with Band 10 of ASTER TIR at 8.2 μm (red line) and the least variation is in Band 14 at 11.3μm (green line). The quartz reststrahlen bands show the largest variation with the presence of quartz rich minerals as seen in emissivity measurements of sandy loam soil in Chapter 3, Figure 3. From Figure 19 it can be noticed that for the highest soil moisture conditions on 23rd June 2012 night time, the emissivity is higher in both background as well as anomalous areas compared to all other night time images. The reason could be because of the highest relative soil moisture of 42.91 % found on same 23rd June ASTER TIR which matches with understanding of high emissivity associated with high moisture content (Hulley et al., 2010). Overall the emissivity values for both background and anomalous pixels are above 0.89 and below 0.98. The reasons for the generally high emissivity values can be attributed to the algorithms which were used for creating the Surface emissivity products. The emissivity is derived from atmospherically corrected TIR Radiance products. However, the atmospheric correction algorithms could be based on approximations which lead to a general increase in emissivity in ASTER TIR as compared to laboratory based measurements (Ramsey, 1999). The higher emissivity values could also be attributed to a number of sub pixel components which may be made of different surfaces like bare soil, vegetation, etc. which cause an overall increase in emissivity values for the ASTER 90m TIR scene.

6.4. Discussion on Integration of Synthetic Model & Remote Sensing Results

The input parameters for the synthetic data model were all based on realistic temperature and emissivity sources. Background surface temperature statistics were derived from remotely sensed ASTER satellite images, In situ geothermal hot spot temperatures were collected from ground measurement sources and emissivity measurements were made on real soil types in the laboratory. Although the soil types were not from the study area, nevertheless two different kinds of soils were used as proxy to understand the effect of soil moisture on emitted radiance. Therefore the name 'synthetic data model' seems to be a misnomer. Moreover, sandy loam and loam soils are quite representative of Yellowstone soil types which cover the thermal areas that are rich in quartz and k feldspar minerals. Since the inputs were based on realistic values, the outputs resulting from the model could be compared and possibly even extrapolated to remote sensing results.

The Intermediate Detection Rates from Table 9 from Section 6.2.2 is borrowed into a new Figure 21 consisting of two tables that show the comparison of synthetic data model results (top table) and the remote sensing data results (bottom table) together. A new set of ranks have been assigned to the synthetic data model results based on the separate category of Intermediate detection rates already made in

Table 9. The focus is created on three rows, the top row result from the synthetic data model and the top two row results from the remote sensing results. The cells are pointed out with black arrows with a corresponding description of the scenarios. Such a comparison can only be made between the remote sensing results and the synthetic model results where the soil moisture conditions are uniform over both the background as well as the anomalous pixels. Therefore Figure 21 is a comparison of the most similar results derived from the synthetic model results and the remote sensing results. The top table includes a subset of 8 combinations out of all the 16 combination results from Table 9 from the synthetic model outputs which can be possibly compared with remote sensing results. Remote sensing results are comparable also due to the coarse resolution (25 km) of soil moisture remote sensing data pixel which covers both the thermal area of Sulfur Hills and the background surrounding region providing a single soil moisture condition for both areas as shown in Figure 21 bottom table with SMC % colour coded in blue shades against day and night conditions. The best detection rate from the synthetic data model results in Figure 21 is achieved when the anomalous pixel is covered with dry sandy loam and the background is covered with dry loam (top table, 1st row). The emissivity difference is also shown to be the highest for the same Rank 1 scenario with a value of 0.008 in Band 14 of ASTER TIR in the synthetic model results table. Similarly for the bottom table in Figure 21, the first two rows represent the best surface temperature anomalies with the lowest soil moisture states out of 4 night time ASTER images over Sulfur hills and background area. Although the soil moisture is not 0% in the top two rows nevertheless those are only available for comparison.

Sr.No.	Background Pixels	Anomalous Pixel	Overall Mean Detection Rate	Ranks	Emissivity 11.3 μm Δ
vii (A)	Dry Loam	Dry Sandy Loam	0.745	1	0.008
i (A)	Wet Loam	Wet Loam	0.742	2	0
viii (A)	Wet Loam	Wet Sandy Loam	0.742	2	0.002
i (B)	Dry Loam	Dry Loam	0.741	3	0
viii (B)	Wet Sandy Loam	Wet Loam	0.741	3	-0.002
ii (A)	Wet Sandy Loam	Wet Sandy Loam	0.74	4	0
ii (B)	Dry Sandy Loam	Dry Sandy Loam	0.74	4	0
vii (B)	Dry Sandy Loam	Dry Loam	0.737	5	-0.008

Synthetic Model Results Table

→ **Dry states of two different soils covering background and anomalous pixels showing best detection rate**

Vs

Date	SMC (%)	ASTER Δ °C	Emissivity 11.3μm Δ
8/28/2012 Night	16.4*	12.85	0.03
7/27/2012 Night	34.81	10.96	0.02
6/23/2012 Night	42.91	10.59	0.01
7/11/2012 Night	36.35	9.19	0.02
9/18/2012 Day	15.48	7.70	0.01
8/17/2012 Day	0	6.92	0.01
6/30/2012 Day	22.08	5.00	0.01

Remote Sensing Results Table

→ **Driest conditions in Sulfur Hills and Background region showing largest anomalies Δ °C**

Figure 21 Comparison of Synthetic Data Model & Remote Sensing Results. The table on the top shows the synthetic data model results borrowed from Table 9 with only the Intermediate Detection Rates. The Sr. No. column stands for the serial number of Table 5 and Figure 11 anomaly detection plots in Chapter 4, Section 4.4.4. The Ranks column is colour coded with the best detection rates corresponding to the green colour and the worst detection rates corresponding to the red colour. The column of Emissivity Δ stands for the emissivity value difference between the anomalous pixel and the background pixel in Band 14 of ASTER TIR at 11.3μm wavelength. The bottom table is the same table from Table 8 which shows the summary of surface temperature anomalies and soil moisture information corresponding to each 7 day and night ASTER images of Sulfur Hills.

From the comparison of the best anomaly detection combination result in the synthetic model table in Figure 21 to the top two night time remote sensing surface temperature anomaly results indicate that when the conditions are dry over both the anomalous area and the background area (dry sandy loam and dry loam respectively) the emitted radiance contrast is better than the when the conditions are wet. This is also determined by the emissivity difference which is shown by the positive difference of emissivity in Band 14 11.3 μm of ASTER TIR. Dry Sandy Loam has a higher emissivity in 11.3μm than Dry Loam at the same wavelength. Therefore, the anomalous pixel which is at higher temperature and higher emissivity shows a better elevated emitted radiance as compared to the dry loam with lower emissivity and lower surface temperature covering the background area. For the remote sensing results, the surface temperature anomalies 12.85°C and 10.96°C for two night time conditions show that when the relative surface soil moisture is low out of 4 night time scenes, the best thermal anomaly detection are achieved. This is possible because when the soil moisture conditions are low the emitted radiance contrast is better developed than when the conditions are wet over both the areas.

Although other rows of results are included in the tables of Figure 21, they are not discussed in order to only focus on the highlighted results. The Day time images are not included for comparison.

The areas of uncertainties in comparison of the synthetic data model results to the remote sensing results are the comparison between the high accuracy, high precision soil moisture data used for from synthetic data model results and the low accuracy, low precision soil moisture information from remote sensing results.

6.5.   Discussion on Limitations and Uncertainties Applied in Remote Sensing Analysis

The source of Soil Moisture data is ASCAT (Advanced scatterometer) sensor on Metop-A satellite with a Spatial Resolution of 25km (spatial sampling 12.5 km) (Wien, 2015). Therefore the relative surface soil moisture information (0% dry and 100% wet) may not be uniformly distributed all throughout the pixel because there are errors associated with each retrieval. This is an approximation of the soil moisture data retrieval algorithm (Wien, 2015). The largest uncertainties exist due to the time gap between the acquisition of ASTER scene over Yellowstone during the night and the ASCAT Metop relative soil moisture retrievals. Since the time differences are of the order of 5 hrs to 18 hrs, there is some difficulty in assuming that the soil moisture states retrieved at the time of ASCAT is the same when the ASTER Images are acquired. But the amount of rainfall during the particular day can provide some clues whether soil moisture increased, decreased or remained constant. Precipitation is not the only source of soil moisture, as there can be other sources such as ground water, moisture brought out by geothermal activity.

Background area digitization can be quite subjective when assuming that the land cover is made of similar composition because it is hard to figure out where the boundary of the area with uniform composition begins and ends given the 90 m pixel size of ASTER. In reality the land cover composition can be gradational. The background area delineation was visually made based on Google Earth Satellite Images and ancillary information.

6.6.   Discussion on Geothermal Anomaly Definition

This is a discussion on the geothermal anomaly definition.
Geothermal anomalies can be sub-pixel in sizes however, no direct high resolution (<3m) thermal infrared data was available to make a detailed assessment of typical sizes and temperature differences of geothermal

anomalies found in Olkaria and Yellowstone. The In situ hot spot geothermal surface temperatures for Olkaria and Yellowstone ranged from >10°C to ~94°C. The mean background surface temperature for Yellowstone was 9°C for night time images. From the 16 combinations of anomaly detection based on the dry and wet soil emissivity, the best detection rates and the worst detection rates are used as a reference for creating a graphical representation of the overall range of results in Figure 22. The Figure consists of a horizontal axis with the units in degree Celsius of the temperature difference between the background of 9°C and the range of hot spot temperature from 20°C to 94°C. Therefore the first value on the horizontal axis shows a difference of 20°C-9°C = 11°C followed by 30-9=21°C and so on. The vertical axis shows the hot spot temperature pixel fraction. The area within the two red and blue regions on the graph shows the space for no detection. The bordering dashed red and blue lines are the minimum limits of thermal anomaly detection. The white space above the minimum detection limit is the area of successful anomaly detection region. The best and worst anomaly detection scenario are taken from the best and worst anomaly detection plots out of 16 combinations of dry and wet soils for Yellowstone night time. This graphical representation helps to explain the effect of hot spot size and pixel fraction on the detection limit of thermal anomalies. For example, if the hot spot temperature is 21°C above the background temperature, it will need at least 40% and above within a pixel shared by the rest 60% background in order to be detectable as a thermal anomaly in the worst detection scenario. Similarly, for a hot spot temperature which is 51°C above the background, it will need to cover at least 20% of the pixel and beyond, shared
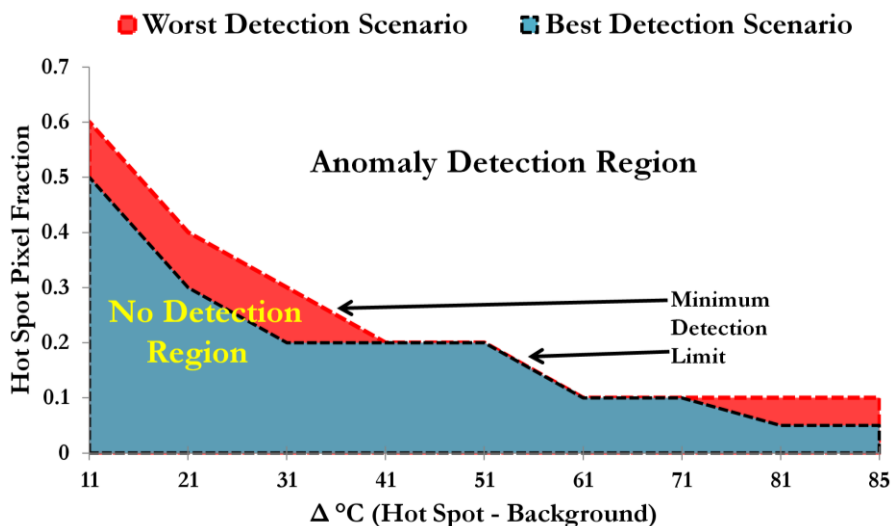
Figure 22 Geothermal anomaly detection limit based on the best and worst detection scenarios

with 80% of the background within a pixel for successful thermal anomaly detection. The criterion for detection remains the same at two times the standard deviation added to the mean background temperature. The significance of this graphical representation is to illustrate that detection behaviour of thermal anomalies are quite non-linear which is in turn dependent on how hot and big a component is within a pixel in order to be detectable. In reality however a pixel may usually be found to be a mixture of several components like bare soil, vegetation and the thermal area. Depending on the properties such as emissivity and the surface temperature of individual components within a pixel, the Pixel integrated radiance will be a sum of average of individual emitted radiance which will influence thermal anomaly detection accordingly. It is useful to consider the aspects of homogeneity of soil moisture within a pixel in order to precisely and accurately detect the thermal anomaly.

7. CONCLUSIONS

Recalling, the general objective of this research was to examine and quantify the effects of soil moisture on geothermal surface temperature anomalies. The research objectives were to define a geothermal surface anomaly, perform a synthetic data modelling and remote sensing data analysis to simulate and examine the effects of soil moisture in detecting geothermal surface temperature anomalies. Research questions included typical sizes and temperature differences of geothermal anomalies, parameters related to soil moisture that influence geothermal anomaly detection, effect of sensor noise, differences between day and night, appropriate datasets and study area for testing the results, limitations and uncertainties applied to the remote sensing data analysis. The following section is a summary of answers to the research questions and problems that in turn addresses the research objectives, which ultimately fulfills the general objective of this research.

1. In order to better characterize typical sizes and temperature differences of geothermal anomalies, high resolution thermal infrared data would have been ideal as the anomalies can be sub-pixel in size in ASTER TIR. In the absence of such data, this study utilized a pixel fraction scale of zero to one by incorporating the full range of geothermal hot spot temperatures found in Yellowstone and Olkaria. Detection thresholds of thermal anomalies with respect to pixel fractions show a non-linear behaviour mostly influenced by the variation in emissivity and temperature as shown by the synthetic data model results.

2. The synthetic data model was sufficiently capable of addressing the research objectives by simulating the effects of soil moisture in detecting geothermal surface temperature anomalies. Although there are a number of parameters related to soil moisture which can possibly influence geothermal anomaly detection such as albedo, land surface temperature, emissivity, thermal inertia, latent heat flux only emissivity was looked at in detail. With higher soil moisture content the emissivity increases and when the soil is dry the emissivity is at equilibrium.

3. Night time TIR images are better suited for thermal anomaly detection than day time images as revealed by the synthetic data modelling and remote sensing results. In addition the conditions of the sky should be clear with least cloud cover percentage preferably with 0% cloud cover over the area of interest while acquiring TIR Images. Soil moisture conditions associated with TIR Images can be extracted from soil moisture retrieving satellite data over the thermal and background area with close proximity to TIR data acquisition time. There are limitations to spatial resolution of soil moisture data used in this study in addition to data gaps. The data gaps could have been replaced by soil moisture information from other satellites instead of interpolation.

4. The ASTER TIR sensor noise had negligible effect on the anomaly detection rates.

5. The synthetic modelling results showed that the best thermal anomalies can be expected in thermal infrared data in the 8 to 12 μm range when the thermal area and the background area is made of two different kinds of surface materials. Ideally, if the thermal area has a higher surface temperature and higher emissivity (high moisture content) in comparison to the background area with lower surface temperature and lower emissivity (low moisture content), the best detection possibility can be expected. Greater the difference between the emitted radiance of thermal area and background area, better will be the contrast developed leading to better detection rates.

6. The worst thermal anomaly detection rates in ASTER TIR can be expected when the background has a surface temperature which is closer to the thermal surface temperature with higher emissivity than the emissivity of thermal features. The emitted radiance contrast between the thermal area and the background area is not developed clearly in this case.

7. Intermediate thermal anomaly detection rates in ASTER TIR can be expected when both the background as well as the thermal area is made of same kind of surface material with the same emissivity (same soil moisture states) but different surface temperatures.

8. The remote sensing time series results showed that when both the thermal and background area are covered by relatively dry conditions equally, the surface temperature anomalies are conspicuous. Individual soil moisture conditions prevailing over the background and thermal area cannot be determined separately from the current ASCAT Metop Soil moisture data with a resolution of 25km. Therefore, only those modelled results could be compared with the remote sensing results where the soil moisture condition of background and anomalous area are the same. There was some agreement between the modelled and remote sensing results when the anomalous and background pixels were dry.

9. Uncertainties are mainly associated with the differences in time of remote sensing data retrieval from ASCAT Metop and ASTER, large difference in spatial resolutions of 25km and 90m, algorithm used for the estimation of surface temperature, atmospheric correction algorithms used for generating Surface Emitted Radiance ordered from LPDAAC for ASTER, background area digitization in ASTER Images, experimental setup for emissivity measurements and systematic errors related to FTIR. Limitations of the study include non-availability of high resolution thermal infrared data for geothermal area characterization. It is a rarity to find cloud free images immediately after a precipitation event, even rarer to find cloud free day and night image pairs for the same day over Yellowstone.

10. The methods applied in this study can be applied to any other geothermal area on earth, provided there are cloud free TIR day and night images, in situ hot spot geothermal temperature information, availability of soil moisture data with highest spatial and temporal resolutions over the thermal and background area with close proximity to TIR data retrieval time. It is not necessary to wait for acquiring an ASTER TIR image immediately after a precipitation event. Any cloud free ASTER TIR image acquired over a geothermal area can be analyzed for the soil moisture states over the top few micrometers or centimetres of the soil surface by comparing with a satellite soil moisture data.

8. RECOMMENDATIONS

Following are some of the recommendations to improve this study and a perspective on future outlook:

1. In order to choose realistic pixel fractions for thermal anomaly definition, high resolution thermal infrared data (<3m) over known geothermal areas can be examined.
2. It would be beneficial to compare the results of thermal anomaly detection carried out during dawn and night, if such a possibility exists. Dawn time can show better results due to minimum insolation effects.
3. The NEdT of ASTER TIR subsystem can be compared from a time period at the beginning of the mission (Year 2000) to the present time (Year 2016) to identify more precisely if the sensor noise has any adverse effect on the anomaly detection due the aging of the sensor.
4. Emissivity Normalization is just one of the methods to estimate the surface temperature of a radiance image by making a reasonable assumption of an emissivity of 0.96. However, there are other methods which can be used to estimate the surface temperature such as Alpha Residuals, Reference Channel, Temperature Emissivity Separation method, etc. It would be interesting to find how different methods influence the results of the synthetic model.
5. The Synthetic Model can be extended to examine the influence of other parameters such as land surface temperature, albedo, thermal inertia, latent heat fluxes due to variations in soil moisture. The synthetic data model can be used with the emissivity of any type of soil, measured In Situ or in the lab, disturbed or undisturbed, dry, wet or intermediate soil moisture conditions using a thermal infrared spectrometer and can thus be extended to test the actual soil types present in Yellowstone, Olkaria or any other geothermal area on the earth to precisely quantify the thermal anomalies influenced by soil moisture. The synthetic data analysis did not deal specifically with situations when false positives appear in the background area. Therefore this is another area which requires further attention and extension to the synthetic model.
6. With the advent of the highest spatial resolution (3/9/36 km) soil moisture retrieving SMAP satellite, the influence of soil moisture on anomaly detection can be better constrained. Therefore it is highly recommended to utilize SMAP soil moisture data along with ASTER TIR for thermal anomaly detection.
7. This study did not take into account geothermal heat fluxes and false anomaly removal from day time or night time images because the aim was to see the influence of soil moisture on anomaly detection. Future work can include these parameters.
8. Extensive time series analysis could provide more information on change of LST due to different factors (solar angle, soil moisture, albedo, etc.), to improve understanding of geothermal areas in ASTER TIR Images. This study only used limited number of ASTER Images.
9. The findings of this study have possible applications in the initial geothermal energy exploration stage. Specifically, to make decisions for selecting TIR data from appropriate time, by taking into consideration the soil moisture conditions prevailing over a potentially viable geothermal region.
10. Multiple applications can be anticipated with the effect of soil moisture on thermal anomalies related to volcano monitoring, earthquake precursors, forest burns and environmental impacts.

LIST OF REFERENCES

Abrams, M., Tsu, H., Hulley, G., Iwao, K., Pieri, D., Cudahy, T., & Kargel, J. (2015). The Advanced Spaceborne Thermal Emission and Reflection Radiometer (ASTER) after fifteen years: Review of global products. *International Journal of Applied Earth Observation and Geoinformation*, *38*, 292–301. doi:10.1016/j.jag.2015.01.013

Bank, W. (2016). Kenya. Retrieved February 15, 2016, from http://sdwebx.worldbank.org/climateportal/index.cfm?page=country_historical_climate&ThisRegion=Africa&ThisCCode=KEN

Bergfeld, D., Lowenstern, J., Hunt, A., Shanks III, W., & Evans, W. (2011). Gas and Isotope Chemistry of Thermal Features in Yellowstone National Park, Wyoming. *U.S Geological Survey Scientific Investigations Report*, (September), 5012. doi:10.3133/sir20115012

Calvin, W., Coolbaugh, M., & Kratt, C. (2005). Application of remote sensing technology to geothermal exploration. In H. N. Rhoden, R. C. Steininger, & P. G. Vikre (Eds.), *Geological Society of Nevada Symposium 2005: Window to the World* (pp. 1083–1089). Reno, Nevada.

Calvin, W., Coolbaugh, M., & Vaughan, R. G. (2002). Geothermal Site Characterization Using Multi- and Hyperspectral Imagery Acknowledgments. *GRC Transactions*, *26*, 483–484.

Coolbaugh, M. F., Kratt, C., Fallacaro, A., Calvin, W. M., & Taranik, J. V. (2007). Detection of geothermal anomalies using Advanced Spaceborne Thermal Emission and Reflection Radiometer (ASTER) thermal infrared images at Bradys Hot Springs, Nevada, USA. *Remote Sensing of Environment*, *106*(3), 350–359. doi:10.1016/j.rse.2006.09.001

Davies, A. G., Calkins, J., Scharenbroich, L., Vaughan, R. G., Wright, R., Kyle, P., … Tran, D. (2008). Multi-instrument remote and in situ observations of the Erebus Volcano (Antarctica) lava lake in 2005: A comparison with the Pele lava lake on the jovian moon Io. *Journal of Volcanology and Geothermal Research*, *177*(3), 705–724. doi:10.1016/j.jvolgeores.2008.02.010

Dehn, J., Dean, K. G., Engle, K., & Izbekov, P. (2002). Thermal precursors in satellite images of the 1999 eruption of Shishaldin Volcano. *Bulletin of Volcanology*, *64*(8), 525–534. doi:10.1007/s00445-002-0227-0

Elachi, C., & Zyl, J. van. (1987). *Introduction to the physics and techniques of remote sensing.* (J. A. Kong, Ed.) (Second.). New Jersey: WILEY-INTERSCIENCE. doi:10.1016/0031-9201(89)90201-X

Eneva, M., & Coolbaugh, M. (2009). Importance of Elevation and Temperature Inversions for the Interpretation of Thermal Infrared Satellite Images Used in Geothermal Exploration. *GRC Transactions*, *33*, 467–470.

Eneva, M., Coolbaugh, M., Bjornstad, S. C., & Combs, J. (2007). In search for thermal anomalies in the Coso gothermal field (California) using remote sensing and field data. In *Thirty-Second Workshop on Geothermal Reservoir Engineering, Stanford University*. California.

Eneva, M., Coolbaugh, M., & Combs, J. (2006). Application of Satellite Thermal Infrared Imagery to Geothermal Exploration in East Central California. *GRC Transactions*, *30*, 407–412.

Gillespie, A., Rokugawa, S., Matsunaga, T., Steven Cothern, J., Hook, S., & Kahle, A. B. (1998). A temperature and emissivity separation algorithm for advanced spaceborne thermal emission and reflection radiometer (ASTER) images. *IEEE Transactions on Geoscience and Remote Sensing*, *36*(4), 1113–1126. doi:10.1109/36.700995

Gupta, R. P. (2003). Chapter 9: Interpretation of data in the Thermal Infrared Region. In *Remote Sensing Geology* (Second Edi.). Heidelberg: Springer.

Gutiérrez, F. J., Lemus, M., Parada, M. a., Benavente, O. M., & Aguilera, F. a. (2012). Contribution of ground surface altitude difference to thermal anomaly detection using satellite images: Application to volcanic/geothermal complexes in the Andes of Central Chile. *Journal of Volcanology and Geothermal Research*, *237-238*, 69–80. doi:10.1016/j.jvolgeores.2012.05.016

Haselwimmer, C., & Prakash, A. (2013). Thermal Infrared Remote Sensing. In C. Kuenzer & S. Dech (Eds.), *Thermal Infrared Remote Sensing: Sensors, Methods, Applications* (Vol. 17, pp. 453–473). doi:10.1007/978-94-007-6639-6

Heasler, H., Jaworowski, C., & Foley, D. (2009). Geothermal systems and monitoring hydrothermal features. In *Geological Monitoring* (pp. 105–140). Boulder: Geological Society of America. doi:10.1130/2009.monitoring(05).

Hecker, C., Hook, S., van der Meijde, M., Bakker, W., van der Werff, H., Wilbrink, H., … van der Meer, F.

(2011). Thermal infrared spectrometer for Earth science remote sensing applications-instrument modifications and measurement procedures. *Sensors*, *11*(11), 10981–99. doi:10.3390/s111110981

Hochstein, M. P., & Dickinson, D. J. (1970). Infra-red remote sensing of thermal ground in the Taupo region, New Zealand. *Geothermics*, *2*, 420–423. doi:10.1016/0375-6505(70)90039-8

Hodder, D. T. (1970). Application of remote sensing to geothermal prospecting. *Geothermics*, *2*(2), 368–380. doi:10.1016/0375-6505(70)90035-0

Hulley, G. C., Hook, S. J., & Baldridge, A. M. (2010). Investigating the effects of soil moisture on thermal infrared land surface temperature and emissivity using satellite retrievals and laboratory measurements. *Remote Sensing of Environment*, *114*(7), 1480–1493. doi:DOI: 10.1016/j.rse.2010.02.002

Jaworowski, C., Heasler, H. P., Neale, C. M. U., & Sivarajan, S. (2010). Using thermal infrared imagery and LiDAR in Yellowstone geyser basins. *Yellowstone Science*, *18*(1), 8–19.

JPL. (2003). Baseline Performance. Retrieved December 24, 2015, from http://www.science.aster.ersdac.jspacesystems.or.jp/t/en/documnts/users_guide/part1/02_02.html

Kealy, P. S., & Hook, S. J. (1993). Separating Temperature and Emissivity in Thermal Infrared Multispectral Scanner Data: Implications. *IEEE Transactions on Geoscience and Remote Sensing*, *31*(6), 1155–1164. doi:0196289293

Kuenzer, C., & Dech, S. (Eds.). (2013). *Thermal Infrared Remote Sensing: Sensors, Methods, Applications* (Vol. 17). Dordrecht Heidelberg New York London. doi:10.1007/978-94-007-6639-6

Ledgard, M. B. (1989). Geothermal Activity and Structure of Longonot Volcano, the Greater Olkaria and Eburru Volcanic Complexes, and Adjacent Areas. Government of Kenya.

Li, Z.-L., Tang, B.-H., Wu, H., Ren, H., Yan, G., Wan, Z., … Sobrino, J. a. (2013). Satellite-derived land surface temperature: Current status and perspectives. *Remote Sensing of Environment*, *131*, 14–37. doi:10.1016/j.rse.2012.12.008

Macgregor, D. (2015). History of the development of the East African Rift System: A series of interpreted maps through time. *Journal of African Earth Sciences*, *101*, 232–252. doi:10.1016/j.jafrearsci.2014.09.016

MCG, C., DG, W., D, A., & G, D. (1990). *Geological, Volcanological and Hydrogeological Controls on the Occurrence of Geothermal Activity in the Area Surrounding Lake Naivasha, Kenya*. British Geological Survey. Retrieved from https://searchworks.stanford.edu/view/2245812

Mira, M., Valor, E., Boluda, R., Caselles, V., & Coll, C. (2007). Influence of soil water content on the thermal infrared emissivity of bare soils: Implication for land surface temperature determination. *Journal of Geophysical Research*, *112*(F4), F04003. doi:10.1029/2007JF000749

Mongillo, M. (1994). Aerial thermal infrared mapping of the Waimangu-Waiotapu geothermal region, New Zealand. *Geothermics*, *23*(5-6), 511–526. doi:10.1016/0375-6505(94)90016-7

Moore, J., Ross P., H., Wright Michael, P., Nichols R., C., Kasameyer, P., Livermore, L., … Battocletti C., E. (2006). *Exploration 1976 - 2006: A History of Geothermal Energy Research and Development in the United States*.

Murphy, S. W., Filho, C. R. D. S., & Oppenheimer, C. (2011). Monitoring volcanic thermal anomalies from space: Size matters. *Journal of Volcanology and Geothermal Research*, *203*(1-2), 48–61. doi:10.1016/j.jvolgeores.2011.04.008

NPS. (2016). Yellowstone. Retrieved February 15, 2016, from http://www.nps.gov/yell/planyourvisit/weather.htm

Parks, J. (2016). Yellowstone National Park. Retrieved July 14, 2016, from http://www.nps.gov/yell/index.htm

Pergola, N., D'Angelo, G., Lisi, M., Marchese, F., Mazzeo, G., & Tramutoli, V. (2009). Time domain analysis of robust satellite techniques (RST) for near real-time monitoring of active volcanoes and thermal precursor identification. *Physics and Chemistry of the Earth*, *34*(6-7), 380–385. doi:10.1016/j.pce.2008.07.015

Pieri, D., & Abrams, M. (2005). ASTER observations of thermal anomalies preceding the April 2003 eruption of Chikurachki volcano, Kurile Islands, Russia. *Remote Sensing of Environment*, *99*(1-2), 84–94. doi:10.1016/j.rse.2005.06.012

Qin, Q., Zhang, N., Nan, P., & Chai, L. (2011). Geothermal area detection using Landsat ETM+ thermal infrared data and its mechanistic analysis-A case study in Tengchong, China. *International Journal of Applied Earth Observation and Geoinformation*, *13*(4), 552–559. doi:10.1016/j.jag.2011.02.005

Ramsey, M. S. (1999). Quantitative Geological Surface Processes Extracted from Infrared Spectroscopy and Remote Sensing. In *Infrared* (pp. 1–17). Retrieved from http://www.pitt.edu/~mramsey/papers/GAC1.pdf

Ranz, P. (2015). GIS Data. Retrieved December 28, 2015, from http://www.wsgs.wyo.gov/pubs-maps/gis

Reath, K. a., & Ramsey, M. S. (2013). Exploration of geothermal systems using hyperspectral thermal infrared remote sensing. *Journal of Volcanology and Geothermal Research*, *265*, 27–38. doi:10.1016/j.jvolgeores.2013.08.007

Salisbury, J. W., & D'Aria, D. M. (1992). Infrared (8-14 gm) Remote Sensing of Soil Particle Size. *Remote Sensing of Environment*, *42*, 157–165.

Sanchez, J. M., French, A. N., Mira, M., Hunsaker, D. J., Thorp, K. R., Valor, E., & Caselles, V. (2011). Thermal Infrared Emissivity Dependence on Soil Moisture in Field Conditions. *IEEE Transactions on Geoscience and Remote Sensing*, *49*(11), 4652–4659. doi:10.1109/TGRS.2011.2142000

Sully, J., Jay, Z., & Inskeep, W. (2015). Yellowstone National Park Research Coordination Network. Retrieved December 24, 2015, from http://rcn.montana.edu/

Tianyu, L., Guonian, L., & Yongning, W. (2012). Application of land surface temperature inversion based on emissivity mixture analysis at sub-pixel scale in geothermal exploration_Tianyu, Guonian, Yongning_2012_2012 Second International Workshop on Earth Observation and.pdf. In *Second International Workshop on Earth Observation and Remote Sensing Applications*. IEEE.

UNEP. (2015). COP 21. Retrieved January 7, 2016, from http://www.cop21paris.org/

van der Meer, F., Hecker, C., van Ruitenbeek, F., van der Werff, H., de Wijkerslooth, C., & Wechsler, C. (2014). Geologic remote sensing for geothermal exploration: A review. *International Journal of Applied Earth Observation and Geoinformation*, *33*(1), 255–269. doi:10.1016/j.jag.2014.05.007

Vaughan, R. G., Heasler, H., Jaworowski, C., Lowenstern, J. B., & Keszthelyi, L. P. (2014). *Provisional Maps of Thermal Areas in Yellowstone National Park , based on Satellite Thermal Infrared Imaging and Field Observations Scientific Investigations Report 2014 – 5137*. Reston, Virginia. Retrieved from http://dx.doi.org/10.3133/sir20145137

Vaughan, R. G., & Hook, S. J. (2006). Using satellite data to characterize the temporal thermal behavior of an active volcano: Mount St. Helens, WA. *Geophysical Research Letters*, *33*(20), 94–97. doi:10.1029/2006GL027957

Vaughan, R. G., Kervyn, M., Realmuto, V., Abrams, M., & Hook, S. J. (2008). Satellite measurements of recent volcanic activity at Oldoinyo Lengai, Tanzania. *Journal of Volcanology and Geothermal Research*, *173*(3-4), 196–206. doi:10.1016/j.jvolgeores.2008.01.028

Vaughan, R. G., Keszthelyi, L. P., Davies, A. G., Schneider, D. J., Jaworowski, C., & Heasler, H. (2010). Exploring the limits of identifying sub-pixel thermal features using ASTER TIR data. *Journal of Volcanology and Geothermal Research*, *189*(3-4), 225–237. doi:10.1016/j.jvolgeores.2009.11.010

Vaughan, R. G., Keszthelyi, L. P., Lowenstern, J. B., Jaworowski, C., & Heasler, H. (2012). Use of ASTER and MODIS thermal infrared data to quantify heat flow and hydrothermal change at Yellowstone National Park. *Journal of Volcanology and Geothermal Research*, *233-234*, 72–89. doi:10.1016/j.jvolgeores.2012.04.022

Wang, H., Xiao, Q., Li, H., Du, Y., & Liu, Q. (2015). Investigating the Impact of Soil Moisture on Thermal Infrared Emissivity Using ASTER Data, *12*(2), 294–298.

Wessels, R. L., Vaughan, R. G., Patrick, M. R., & Coombs, M. L. (2013). High-resolution satellite and airborne thermal infrared imaging of precursory unrest and 2009 eruption at Redoubt Volcano, Alaska. *Journal of Volcanology and Geothermal Research*, *259*, 248–269. doi:10.1016/j.jvolgeores.2012.04.014

Wien, T. (2015). Metop ASCAT Soil Moisture DataViewer. Retrieved December 28, 2015, from http://rs.geo.tuwien.ac.at/dv/ascat/